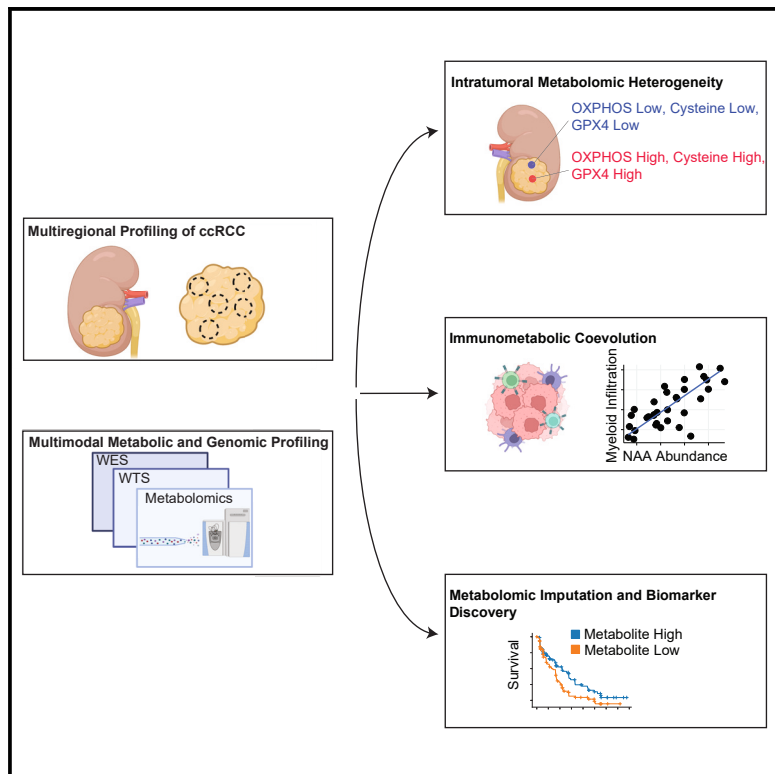


## Immunometabolic coevolution defines unique microenvironmental niches in ccRCC

### Graphical abstract



### Authors

Cerise Tang, Amy X. Xie,  
Eric Minwei Liu, ..., Nikolaus Schultz,  
A. Ari Hakimi, Ed Reznik

### Correspondence

hakimia@mskcc.org (A.A.H.),  
reznike@mskcc.org (E.R.)

### In brief

Using multimodal metabolic profiling, Tang et al. show that intratumoral metabolomic heterogeneity in clear cell renal cell carcinoma (ccRCC) is driven by the oxidative stress response and coevolves with specific patterns of immune infiltration.

### Highlights

- Spatial, multimodal measurements of ccRCC metabolism and microenvironment
- ccRCC demonstrates a pattern of ferroptosis-associated intratumoral heterogeneity
- Local metabolomic phenotypes associate with specific patterns of immune infiltration
- Discovery of metabolite biomarkers of therapy response via RNA-metabolite covariation



Article

# Immunometabolic coevolution defines unique microenvironmental niches in ccRCC

Cerise Tang,<sup>1,2</sup> Amy X. Xie,<sup>1,3</sup> Eric Minwei Liu,<sup>1</sup> Fengshen Kuo,<sup>4</sup> Minsoo Kim,<sup>1</sup> Renzo G. DiNatale,<sup>1</sup> Mahdi Golkaram,<sup>5</sup> Ying-Bei Chen,<sup>6</sup> Sounak Gupta,<sup>6</sup> Robert J. Motzer,<sup>7</sup> Paul Russo,<sup>4</sup> Jonathan Coleman,<sup>4</sup> Maria I. Carlo,<sup>7</sup> Martin H. Voss,<sup>7</sup> Ritesh R. Kotecha,<sup>7</sup> Chung-Han Lee,<sup>8</sup> Wesley Tansey,<sup>1</sup> Nikolaus Schultz,<sup>1</sup> A. Ari Hakimi,<sup>4,10,\*</sup> and Ed Reznik<sup>1,9,11,\*</sup>

<sup>1</sup>Computational Oncology, Memorial Sloan Kettering Cancer Center, New York, NY, USA

<sup>2</sup>Physiology, Biophysics and Systems Biology Graduate Program, Weill Cornell Medicine, New York, NY, USA

<sup>3</sup>Biochemistry, Structural Biology, Cell Biology, Developmental Biology and Molecular Biology Graduate Program, Weill Cornell Medicine, New York, NY, USA

<sup>4</sup>Urology Service, Department of Surgery, Memorial Sloan Kettering Cancer Center, New York, NY 10065, USA

<sup>5</sup>Illumina, Inc., 5200 Illumina Way, San Diego, CA 92122, USA

<sup>6</sup>Department of Pathology, Department of Medicine, Memorial Sloan Kettering Cancer Center, New York, NY, USA

<sup>7</sup>Genitourinary Oncology Service, Department of Medicine, Memorial Sloan Kettering Cancer Center, New York, NY, USA

<sup>8</sup>Department of Medicine, Memorial Sloan Kettering Cancer Center, New York, NY 10065, USA

<sup>9</sup>Marie-Josée and Henry R. Kravis Center for Molecular Oncology, Memorial Sloan Kettering Cancer Center, New York, NY 10065, USA

<sup>10</sup>Human Oncology and Pathogenesis Program, Memorial Sloan Kettering Cancer Center, New York, NY 10065, USA

<sup>11</sup>Lead contact

\*Correspondence: hakimia@mskcc.org (A.A.H.), reznike@mskcc.org (E.R.)

<https://doi.org/10.1016/j.cmet.2023.06.005>

## SUMMARY

Tumor cell phenotypes and anti-tumor immune responses are shaped by local metabolite availability, but intra-tumoral metabolite heterogeneity (IMH) and its phenotypic consequences remain poorly understood. To study IMH, we profiled tumor/normal regions from clear cell renal cell carcinoma (ccRCC) patients. A common pattern of IMH transcended all patients, characterized by correlated fluctuations in the abundance of metabolites and processes associated with ferroptosis. Analysis of intratumoral metabolite-RNA covariation revealed that the immune composition of the microenvironment, especially the abundance of myeloid cells, drove intratumoral metabolite variation. Motivated by the strength of RNA-metabolite covariation and the clinical significance of RNA biomarkers in ccRCC, we inferred metabolomic profiles from the RNA sequencing data of ccRCC patients enrolled in 7 clinical trials, and we ultimately identified metabolite biomarkers associated with response to anti-angiogenic agents. Local metabolic phenotypes, therefore, emerge in tandem with the immune microenvironment, influence ongoing tumor evolution, and are associated with therapeutic sensitivity.

## INTRODUCTION

Changes to the metabolism of clear cell renal cell carcinoma (ccRCC) tumors are evolutionarily early events in tumorigenesis that occur in the background of widespread intratumoral genetic diversification and extensive immune infiltration.<sup>1–4</sup> Such metabolic changes, including the upregulation of glucose uptake, increases in anti-oxidant biosynthesis, and the accumulation of lipid droplets, underlie ccRCC malignancy and metastatic competency, and are potentially determinants of response to metabolically targeted therapies.<sup>1,5,6</sup> However, technical challenges associated with the collection of metabolomic data from primary tumors (especially the need for significant amounts of fresh frozen tissue) have precluded both a large-scale analysis of the association of metabolite levels with genomic/microenvironmental tumor features and an assessment of the clinical utility of metabolomic measurements for the prognostication and therapeutic stratification of patients.

The metabolism of ccRCC has overwhelmingly been studied using single-region metabolomic profiling.<sup>1,6–8</sup> However, two emerging hallmarks of ccRCC biology, intratumoral heterogeneity and abundant infiltration by non-malignant immune cells,<sup>2,3</sup> fundamentally confound our understanding of the culprit tumor/non-tumor cell populations driving metabolic phenotypes of interest. Recent work suggests that metabolic heterogeneity (e.g., in PHGDH<sup>9</sup> and MCT1<sup>10</sup>) can mechanistically influence the competency of tumor cells to metastasize, supporting a rational therapeutic strategy that limits heterogeneity or targets heterogeneous pathways supporting aggressive behavior. However, the aforementioned studies do not address the full extent of tumor cell-intrinsic metabolic heterogeneity in human cancers. Furthermore, these phenomena imply that the hallmark features of ccRCC metabolism discovered through measurements of cellularly heterogeneous bulk tumors, including aerobic glycolysis and the upregulation of the anti-oxidant response, are themselves heterogeneous and vary significantly across the spatial



extent of the tumor. This raises the possibility that some ccRCC metabolic phenotypes arise either directly from non-tumor cells or indirectly via the metabolic reprogramming of tumor cells in specific immune microenvironments. However, existing studies of intratumoral metabolomic heterogeneity (IMH) in ccRCC have been limited to small numbers (typically, two) of tumor regions<sup>11,12</sup> and have largely lacked the orthogonal measurements of the genome, transcriptome, and microenvironment necessary to test this hypothesis. Thus, neither the intratumoral heterogeneity of metabolic phenotypes nor their cellular source (i.e., from tumor or immune cells) are well understood.

Here, to characterize metabolic intratumor heterogeneity and its drivers, we assembled a cohort of 123 tumor and 64 adjacent normal regions from 31 ccRCC patients with associated metabolomic, genomic, and transcriptomic profiling. Through the analysis of this spatial, multimodal dataset, we discovered that elevated IMH was associated with specific transcriptomic and immunologic features, including lower cytotoxic cell infiltration, but comparatively few distinguishing genomic features. Joint analysis of the entire dataset revealed that all patients evolved a similar pattern of IMH dominated by a metabolic program resembling compensation to ferroptotic susceptibility, with tumor regions primarily stratified by their abundance of cysteine, glutathione, and polyunsaturated fatty acids (PUFAs). Studying in detail the molecular features associated with intratumoral metabolite variation across tumor regions, we found that gene expression profiles associated with immune infiltration and direct measurements of immune cells significantly correlated with the intratumoral variation of numerous metabolites, indicating that the immune microenvironment and metabolism coevolve in ccRCC to produce spatially restricted niches with defined nutrient abundance and immune profiles. Motivated by the strong covariation between the metabolome and transcriptome and the clinical significance of the immune microenvironment in ccRCC, we applied a machine learning algorithm (metabolite imputation via rank-transformation and harmonization [MIRTH]) to impute metabolite levels from RNA sequencing data, ultimately identifying metabolites associated with response to systemic therapy in ccRCC.

## RESULTS

### Multiregional metabolomic, transcriptomic, and genomic profiling of ccRCC

To interrogate metabolomic heterogeneity in RCC, we assembled a mixed cohort of fresh frozen high-quality tumor/adjacent normal specimens covering both (1) patients with only a single region profiled (“single-region”) and (2) patients with multiple tumor and normal regions profiled (“multiregion”). The total cohort included samples from 156 patients, with 33 patients undergoing multiregion profiling. In tumors from treated patients, therapies were administered prior to surgical resection. Metabolomic profiling by mass spectrometry was performed in two batches, with one batch (“M4”) containing 68 patients (18 multiregion) and the other (“M5”) containing 88 patients (15 multiregion). A total of 268 tumor regions and 78 adjacent normal regions were collected. Nivolumab-exposed tumors were profiled 8 weeks after therapy, whereas combination-exposed tumors were profiled an average of 7.5 months after therapy.

Principal component analysis (PCA) of the metabolomics data showed clear separation between tumor and normal samples (Figure S1A). Using a false detection rate (FDR)-corrected Wilcoxon test, we identified 404 and 507 metabolites that display differential abundance (DA) between tumor and normal tissue samples in M4 and M5, respectively, (FDR-adjusted  $p < 0.05$ ), which largely overlapped with previously published data (M1)<sup>1</sup> (Figure S1B). Interestingly, we observed little separation of tumors in PCA based on their exposure to immunotherapy treatment (Figure S1C), and although a small fraction of metabolites (33/602, 6%) demonstrated DA in treated (across all treatment groups) versus untreated tumors (FDR-adjusted  $p < 0.05$ ), these metabolites were not enriched in any one metabolic pathway. These data are consistent with prior knowledge on the relatively limited effect of single-agent Nivolumab on ccRCC gene expression,<sup>13</sup> indicating that exposure to immunotherapy produces (over relatively short clinical time scales) comparatively small metabolomic effects.

To examine the extent of metabolomic heterogeneity across regions and patients, we completed unsupervised hierarchical clustering of metabolomic data across tumor regions (Figure S2A). Consistent with a prior report,<sup>14</sup> the majority of tumor regions clustered by patient of origin in both M4 and M5 cohorts. However, a small number of regions (derived from numerous patients) clustered separately, were distinct in PCA analysis (Figure S2B), and upon inspection were found to have exceptionally low ion counts relative to other tumor samples in the cohort (Wilcoxon  $p = 5 \times 10^{-10}$ ) (Figure S2C). Based on prior literature,<sup>15</sup> we hypothesized that these outlier regions with low ion counts may correspond to the *bona fide* depletion of metabolites resulting from tissue necrosis. DA analysis identified 323 metabolites that distinguish outlier and non-outlier tumor samples (FDR-adjusted  $p < 0.05$  and absolute  $\log_2$  fold change  $> 0.5$ ) (Figure S2D). Interestingly, one of the most upregulated metabolic pathways was sphingomyelins, a lipid species that can be degraded to release pro-apoptotic ceramide molecules<sup>16</sup> (Figures S2E and S2F). Review by an expert pathologist (which we consider the gold standard for necrosis detection) found that 5/5 computationally identified outliers were necrotic, whereas 76/83 non-outliers were found to have no evidence of necrosis (Fisher’s exact test  $p = 2 \times 10^{-5}$ ) (Figure S2G). Necrosis, therefore, is a dominant mode of metabolic heterogeneity in ccRCC whose metabolic characteristics transcend individual patients. For all further analysis, we focused exclusively on multi-region clear cell tumor and normal regions, excluding necrotic regions ( $n = 19$  regions), non-clear patients ( $n = 44$  regions), and single-sample patients ( $n = 98$  regions). This left a total of 31 ccRCC tumors with associated multiregion profiling (123 tumor regions and 64 normal regions; 17 patients in M4 and 14 patients in M5) (Figures 1A and 1B). Details on metabolomic, transcriptomic, and genomic data processing are provided in the STAR Methods.

### The landscape of intratumoral metabolomic heterogeneity in ccRCC

To quantify metabolomic heterogeneity both within and between patients, we calculated an “h-score” for each metabolite corresponding to the expected  $\log_2$  fold change for a given metabolite  $i$  between two randomly chosen regions (Figure S3A).

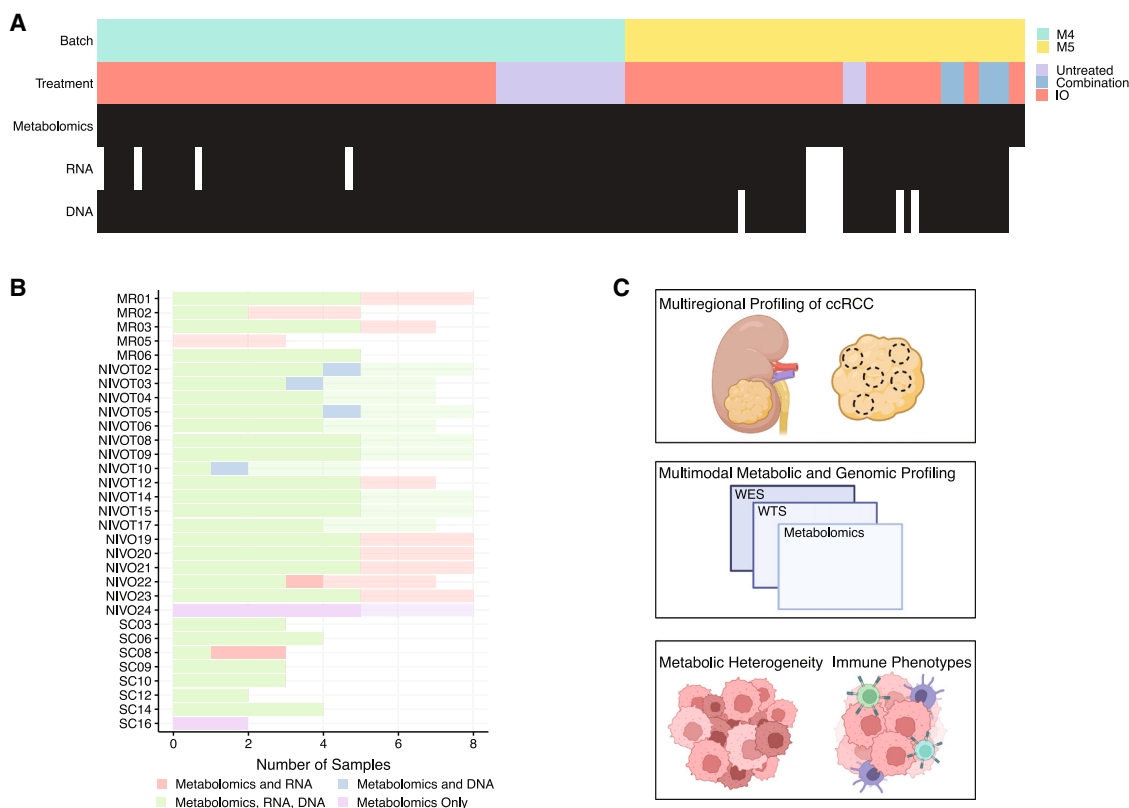


**Figure 1. Clinical and metabolic features of a multimodally profiled cohort of ccRCC tumors**

(A) Overview of 123 tumor regions collected from 31 patients.

(B) Sample breakdown for 31 multiregionally profiled patients. Tumor samples are dark and normal samples are transparent.

(C) Schematic of study workflow showing the collection of multiregional ccRCC samples, followed by multimodal profiling for interrogation of intratumoral metabolomic and microenvironmental heterogeneity.

Summarizing h-scores across all regions of a patient, we found that IMH varied widely by patient: in the most heterogeneous patient (NIVO10), a randomly chosen metabolite could be expected to vary 3-fold between regions, compared with 1.3-fold in the least heterogeneous patient (NIVO4). Interpatient metabolomic heterogeneity was greater than IMH (Figure 2A). Both intrapatient heterogeneity and interpatient heterogeneity were comparable in tumors and its adjacent normal kidney. A small number of metabolites (6%, 54/602) demonstrated differences in their extent of intrapatient metabolomic heterogeneity in tumor compared with normal kidney, but these metabolites were not concentrated in any one pathway. IMH was also not significantly associated with tumor stage (Kruskal-Wallis  $p = 0.45$ ) or grade (Kruskal-Wallis  $p = 0.31$ ).

We hypothesized that elevated IMH may define a class of ccRCC tumors with distinct genomic, transcriptomic, and microenvironmental features. To test this hypothesis, we performed linear regression on the IMH scores of each patient and compared their clinical, metabolomic, transcriptomic, and genomic profiles. There were no significant differences in IMH based on clinical stage ( $p = 0.55$ ) or nuclear grade ( $p = 0.31$ ). Comparing the incidence of key driver mutations in ccRCC (*VHL*, *PBRM1*, *SETD2*, *BAP1*, *KDM5C*, *MTOR*, *TP53*, *PIK3CA*, *TSC2*, *PTEN*, HLA LOH, and *CDKN2A/B* loss), patients with loss of heterozygosity of HLA had higher IMH (median = 0.77)

than patients without HLA LOH (median = 0.64), but this result did not survive multiple hypothesis correction (uncorrected  $p = 0.05$ ) (Figures 2C and 2D). Thus, elevated IMH is not strongly associated with specific genetic alterations in ccRCC tumors.

In contrast, patients demonstrated stark metabolomic differences based on IMH: 137/602 (23%) metabolites significantly correlated with IMH (FDR-adjusted  $p < 0.05$ ), with exceptionally strong enrichment of sphingomyelins (Figure 2B). After controlling for age and sex, we found that significant metabolic correlation with ITH was preserved (Pearson correlation coefficient comparing FDR-adjusted  $p$  values in the two models = 0.95,  $p < 2.2 \times 10^{-16}$ ). Complementary to this, the transcription of 619/19,570 (3%) of genes were significantly associated with patient-level IMH scores (FDR-adjusted  $p < 0.05$ ). Performing gene set enrichment analysis (GSEA), we found that immune pathways (specifically interferon response) were negatively enriched with IMH, whereas pathways associated with cell growth and proliferation were positively enriched (Figure 2E). Comparing the expression of RNA-based immune signatures with IMH, we found statistically significant negative association in cytotoxic cells (FDR-adjusted  $p = 0.04$ ) and Th17 cells (FDR-adjusted  $p = 0.04$ ) (Figure 2F). In total, these data argue that elevated IMH defines a molecularly distinct group of ccRCC tumors with unique metabolic and microenvironmental features but limited differences in genotype.

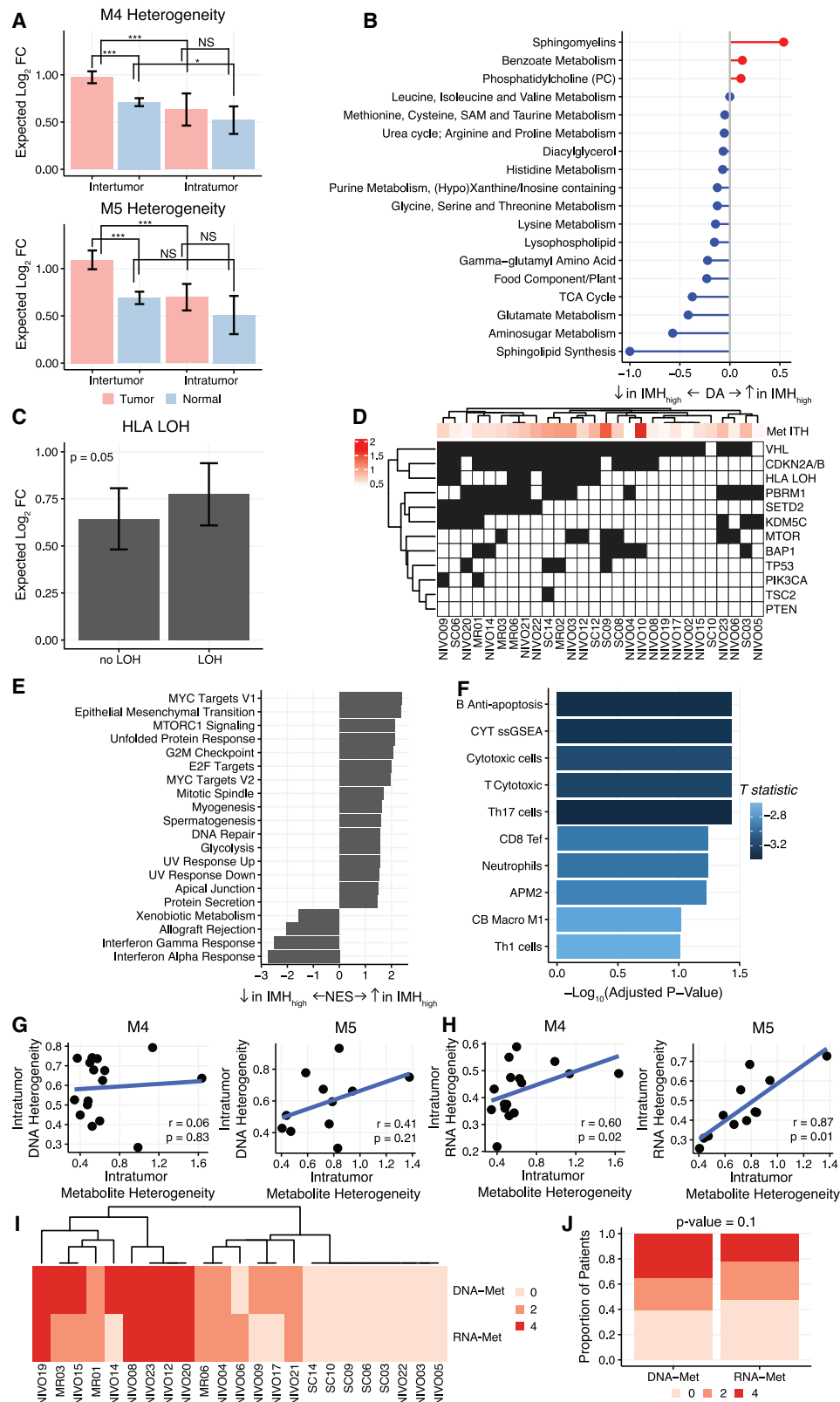


**Figure 2. Tumors with elevated IMH are molecularly distinct**

(A) Barplots comparing levels of interpatient and intrapatient heterogeneity in tumor and normal tissues (\*p < 0.01, \*\*p < 0.0001; NS, not significant). Error bars represent the 95% confidence interval. Heterogeneity values represent log<sub>2</sub> fold abundance difference between two randomly chosen regions.

(legend continued on next page)

### Intratumoral metabolomic evolution mirrors transcriptomic evolution

We considered the possibility that IMH may reflect the overall intratumoral molecular diversity of the whole tumor. To test this, we calculated a measure of intratumoral heterogeneity for matched DNA and RNA sequencing data for 28 patients with sufficient data (number of profiled regions  $\geq 2$ ). Interestingly, the magnitude of patient-specific transcriptomic heterogeneity, but not patient-specific genomic heterogeneity, was correlated to patient-specific metabolomic heterogeneity (transcriptomic heterogeneity, Spearman correlation, M4  $p = 0.02$  and M5  $p = 0.01$ ; genomic heterogeneity, Spearman correlation, M4  $p = 0.83$  and M5  $p = 0.21$ ) (Figures 2G and 2H). Importantly, there was no significant correlation between transcriptomic and genomic heterogeneity (Spearman correlation, M4  $p = 0.55$  and M5  $p = 0.18$ ).

We next investigated the relationship between intratumoral patterns of metabolomic, transcriptomic, and genomic heterogeneity, we reconstructed data-modality-specific evolutionary phylogenies for each patient with at least 3 tumor regions profiled ( $n = 23$  total). By examining the similarity of phylogenies reconstructed from different data modalities (using the Robinson-Foulds metric; [STAR Methods](#)), we observed that in cases where the 3 phylogenetic reconstructions diverged, DNA- and metabolite-based evolutionary phylogenies consistently showed less similarity than RNA- and metabolite-based phylogenies, although this result did not reach statistical significance (paired t test  $p = 0.1$ ) (Figure 2J). Thus, we observed associations in both (1) the magnitude of intratumoral transcriptomic and metabolomic heterogeneity at the level of the whole patient (Figure 2G) and (2) the similarity of transcriptomic/metabolomic profiles between spatially circumscribed tumor regions (Figure 2I), but we failed to observe analogous associations when comparing genomic and metabolomic profiles. The data above thus support a model whereby gene expression and metabolite availability can fluctuate and adapt in response to regional changes in a manner potentially independent of genomic diversification, and they imply that tumor subclones are unlikely to exhibit broad, whole-metabolome differences in phenotypes.

### A heterogeneity program driven by cysteine accumulation, polyunsaturated fatty acids, and ROS tolerance dominates ccRCC tumors

We sought to understand the detailed metabolites and metabolic pathways that ultimately drove IMH across the tumor regions of each patient. To do so, we calculated the IMH of each metabolite in tumor regions ([STAR Methods](#)), focusing special attention on metabolites in glycolysis, the TCA cycle, and other central meta-

bolic pathways that have previously been implicated in the genesis and metastatic progression of ccRCC. Within individual pathways of interest, we observed considerable variation in IMH, with specific metabolites (e.g., glucose-6-phosphate) demonstrating exceptionally high heterogeneity relative to other metabolites in the pathway (Figure 3A). Cysteine was an especially remarkable outlier: the IMH of cysteine was  $>2$ -fold higher than the IMH of any other proteinogenic amino acid (Figures 3A and 3G).

To understand the consequences of elevated heterogeneity in cysteine and other metabolites, we examined correlated intratumoral fluctuations in metabolite levels. Interestingly, after controlling for baseline metabolite abundance in a given patient, we observed highly similar patterns of intratumoral metabolite covariation across patients. For example, across all patients, citrate-high regions in tumors demonstrated consistently higher levels of *cis*-aconitate ( $p < 2 \times 10^{-16}$ ) and lower levels of fumarate ( $p = 6 \times 10^{-9}$ ) than citrate-low regions (Figure 3B). This raised the novel possibility that ccRCC patients evolve a common, universal pattern of IMH, manifesting in correlated fluctuations of metabolites around their baseline level in a patient. To test this hypothesis, we transformed our metabolomic data to capture the fluctuation of each metabolite relative to its mean abundance in a given patient and completed PCA ([STAR Methods](#)). This analysis revealed that the first principal component ("PC1," explaining 26% of the variance in the data) separated tumor and normal regions (Figure 3C) and KEGG-pathway-based analysis showed an enrichment of fatty acids and a decrease in amino acid levels in PC1<sub>high</sub> regions, consistent with prior metabolomic features of ccRCC tumors (Figure S3B).

In contrast to PC1, the second principal component ("PC2," explaining 12% of the variance) separated tumor regions, but not normal regions, from the majority of patients into two distinct classes (Figure 3C). PC2<sub>low</sub> tumor regions demonstrated characteristics associated with elevated uptake and phosphorylation of free glucose (high levels of glucose-6-phosphate) (FDR-adjusted  $p = 1 \times 10^{-5}$ ) and lactate (FDR-adjusted  $p = 0.003$ ) and high levels of the TCA cycle intermediates fumarate (FDR-adjusted  $p = 0.001$ ) and malate (FDR-adjusted  $p = 5 \times 10^{-4}$ ). Additionally, PC2<sub>low</sub> regions also demonstrated higher anti-oxidant levels, including higher reduced glutathione (FDR-adjusted  $p = 0.03$ ), alpha-tocopherol (FDR-adjusted  $p = 0.006$ ), and ascorbate (FDR-adjusted  $p = 3 \times 10^{-4}$ ). In contrast, PC2<sub>high</sub> regions had comparatively higher levels of free glucose (FDR-adjusted  $p = 5 \times 10^{-6}$ ), citrate (FDR-adjusted  $p = 2 \times 10^{-7}$ ), and *cis*-aconitate (FDR-adjusted  $p = 1 \times 10^{-6}$ ), suggesting that these regions are

(B) Pathway-based analysis of metabolic changes associated with IMH. Only pathways with 3 or more metabolites are shown. See [STAR Methods](#).

(C) IMH is weakly elevated in tumors with HLA LOH. Error bars represent the 95% confidence interval.

(D) Driver mutations are not significantly associated with IMH.

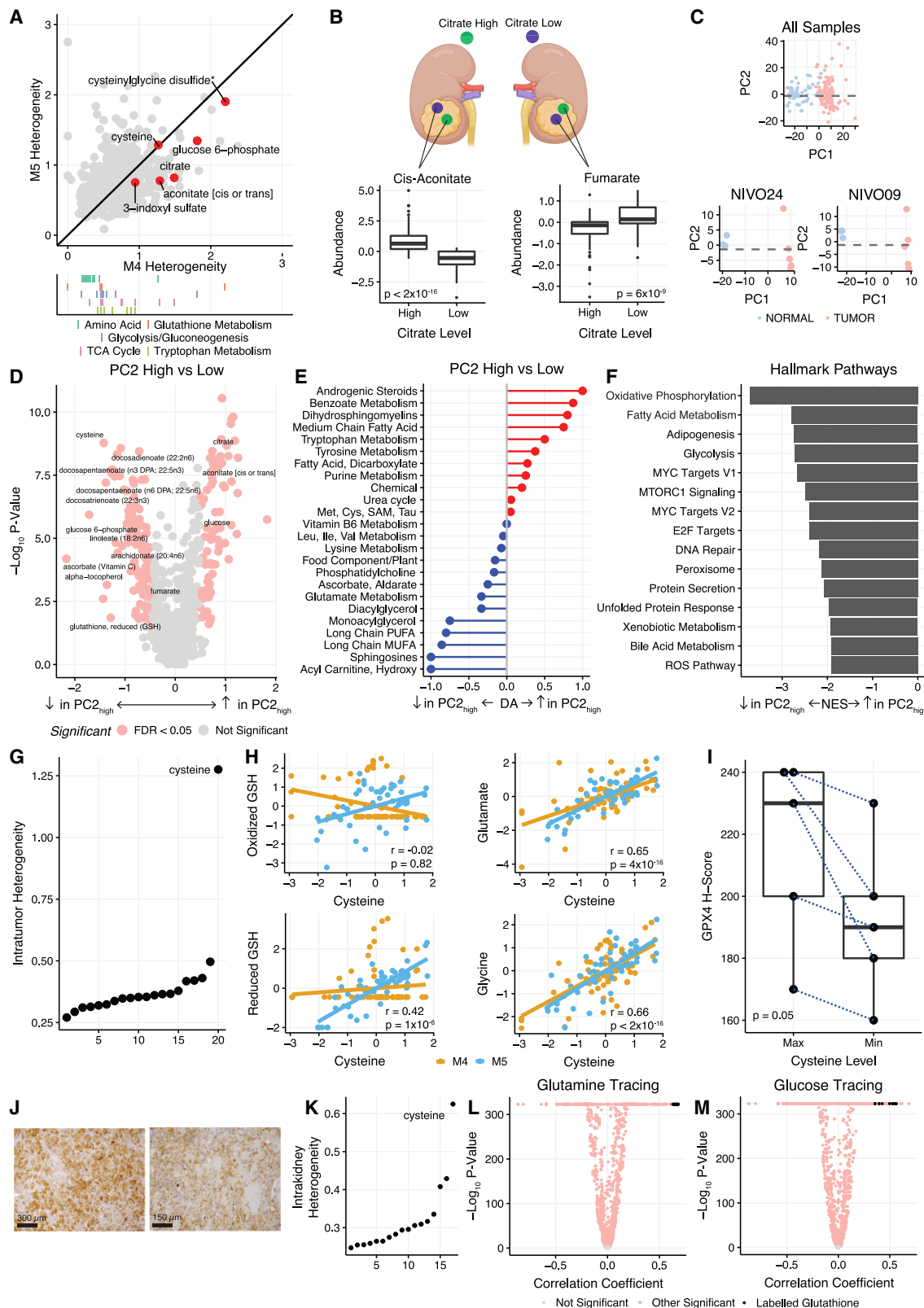
(E) GSEA results of normalized enrichment scores of Hallmark pathways of genes that are significantly associated with IMH calculated using linear regression. All pathways shown are significant (FDR-adjusted  $p < 0.05$ ).

(F) Barplot of  $-\log_{10}$  FDR-adjusted p values comparing immune signature expression based on IMH levels. Numerous immune signatures are depleted in IMH-elevated tumors. Blue color indicates that the fold change between IMH-high and IMH-low tumors is negative.

(G and H) IMH is not significantly correlated to intratumoral genetic diversity (G) but significantly correlated to intratumoral transcriptomic diversity (H) across both batches of metabolomic data (M4 and M5).

(I) Heatmap of Robinson-Foulds distances between DNA, RNA, and metabolite subclonal phylogenies by patient.

(J) Distribution of Robinson-Foulds distances demonstrates that subclonal phylogenies reconstructed from metabolomic and transcriptomic data show a higher degree of similarity than those reconstructed from metabolomic and genomic data.



(legend on next page)

more glucose replete and possibly undergo less aerobic glycolysis (Figure 3D). At a pathway level, PC2<sub>low</sub> tumor regions showed elevation in multiple fatty acid species, including long-chain PUFAs (DA score = -0.8) and hydroxy acylcarnitines (DA score = -1) (Figure 3E), and PC2<sub>low</sub> regions demonstrated a generic tendency to accumulate lipids (Figure S4B). Differential expression of multiregion RNA sequencing data (controlling for patient of origin) found reactive oxygen species (ROS) (FDR-adjusted  $p = 6 \times 10^{-4}$ ) and oxidative phosphorylation (OXPHOS) (FDR-adjusted  $p = 6 \times 10^{-10}$ ) as elevated in PC2<sub>low</sub> tumor regions (Figure 3F). Importantly, we found no significant differences between tumor purity ( $p = 0.8$ ) (Figure S4A) and no significant differences in cellular proliferation as quantified by either RNA signature of proliferation ( $p = 0.31$ ; Figure S4C) or Ki67 staining ( $p = 0.19$ ; Figure S4D). We similarly observed no differences in angiogenesis between regions as evaluated using either an angiogenic RNA signature ( $p = 0.29$ ) or CD31 immunofluorescence staining ( $p = 0.11$ ) (Figures S4E and S4F). These data demonstrate that PC2<sub>low</sub> regions are characterized by elevated rates of glycolysis, high abundance of PUFAs and antioxidants, increased OXPHOS expression, and signatures of elevated ROS production and that the features of PC2<sub>low</sub> regions cannot be explained by changes in tumor cellularity, proliferation, or vascularization.

Among the metabolites with the highest contribution to PC2 were reduced glutathione and its rate-limiting precursor cysteine (Figure S3C), as well as numerous PUFAs. These metabolites are each associated with the molecular process of ferroptosis, an iron-mediated form of cell death triggered by the peroxidation of PUFAs and counteracted by glutathione.<sup>17–20</sup> Based on the data in Figures 3B–3F, we hypothesized that cysteine levels may be elevated in a compensatory manner to produce glutathione and prevent ferroptosis in tumor regions with high PUFA levels and OXPHOS expression. Consistent with this, high tumor cysteine levels were correlated with increased levels of reduced glutathione ( $\rho = 0.42$ ,  $p = 1 \times 10^{-6}$ ), as well as increased levels of the glutathione precursors glutamate ( $\rho = 0.65$ ,  $p = 4 \times 10^{-16}$ ) and glycine ( $\rho = 0.66$ ,  $p < 2 \times 10^{-16}$ ) (Figure 3H), but

no similar effects were observed for the related disulfide cystine (Figures S4G–S4I).

To directly evaluate the functional consequences of cysteine accumulation in tumor regions, we undertook two complementary analyses. First, to understand the functional effects of cysteine on metabolic flux, we leveraged recent spatial metabolomic isotope tracing data from murine kidneys.<sup>21</sup> We recapitulate that, in analogy to Figure 3A, cysteine displays exceptional spatial heterogeneity across the mouse kidney relative to all other proteinogenic amino acids (Figure 3K). Then, by correlating cysteine abundance with labeling patterns from experiments using uniformly labeled glucose and glutamine, we investigated how flux patterns change in cysteine-rich versus cysteine-depleted regions (Figures 3L and 3M). Interestingly, we found that regions with elevated cysteine demonstrated decreased glucose- and glutamine-derived labeling of cysteine (suggesting reduced cysteine biosynthesis and increased *de novo* uptake of cysteine via cystine) and increased glucose-derived and glutamine-derived labeling of glutathione. Together, these data suggest that cysteine-high regions are associated with increased *de novo* uptake of cysteine (e.g., via SLC7A11/cystine), as well as increased flux from extracellular glucose/glutamine to intracellular glutathione biosynthesis. Second, we performed immunohistochemical staining of GPX4, a critical regulator of ferroptotic resistance.<sup>17</sup> For 5 patients, we identified tumor regions demonstrating the highest and lowest abundance of cysteine within a given patient and immunohistochemically stained these regions for GPX4. Consistent with our model above, cysteine-high tumor regions demonstrated elevated GPX4 intensity (paired Wilcoxon  $p = 0.05$ ) (Figures 3I and 3J). Together, these data establish that regions with elevated cysteine levels have distinct metabolic flux patterns and are associated with the upregulation of GPX4. Moreover, these data suggest that PC2<sub>low</sub> regions are defined by an increased susceptibility to ferroptotic cell death (characterized by higher PUFA levels and OXPHOS activity) and concomitant compensation against ferroptosis in the form of upregulated anti-oxidant biosynthesis.

#### Figure 3. A ferroptotic-compensation program underlies IMH in ccRCC

- (A) Top: scatterplot of intratumor heterogeneity of individual metabolites in M4 vs. M5. Bottom: rug plot highlighting metabolites in metabolic pathways of interest.
- (B) Top: schematic demonstrating citrate-high and citrate-low regions within a single tumor. Bottom: boxplots comparing *cis*-aconitate and fumarate levels in citrate-high vs. citrate-low regions.
- (C) Top: PCA of all multiregion samples colored by tumor and normal. Bottom: PCA of samples from single patients, NIVO09 and NIVO24, colored by tumor and normal. PC1 separates tumor and normal samples, whereas PC2 separates tumor regions within individual patients.
- (D) Volcano plot of metabolites differentially expressed in PC2<sub>low</sub> vs. PC2<sub>high</sub> tumor regions colored by significance. Metabolites in red are significant (FDR-adjusted  $p < 0.05$  and absolute  $\log_2$  fold change  $> 0.5$ ).
- (E) Pathway-based analysis of metabolic changes in PC2<sub>high</sub> vs. PC2<sub>low</sub> regions.
- (F) GSEA results comparing PC2<sub>low</sub> with PC2<sub>high</sub> regions. All pathways shown are statistically significant (FDR-adjusted  $p < 0.05$ ).
- (G) Cysteine is exceptional in the magnitude of IMH relative to other proteinogenic amino acids.
- (H) Scatterplots of scaled cysteine abundance vs. oxidized glutathione, reduced glutathione, glutamate, and glycine abundance. Yellow represents samples from the M4 batch, and blue represents samples from the M5 batch.
- (I) Boxplot comparing GPX4 h-scores in maximum cysteine regions vs. minimum cysteine regions. Maximum and minimum samples selected are paired from the same patient. GPX4 protein expression is elevated in cysteine-high regions.
- (J) GPX4 staining of a cysteine maximum (top) region and cysteine minimum (bottom) region from a single patient (MR06). Scale bars represent 300  $\mu\text{m}$  (top) and 150  $\mu\text{m}$  (bottom).
- (K) Intrakidney heterogeneity of amino acids from spatially profiled mouse kidneys.
- (L) Volcano plots from correlating cysteine abundance with labeling patterns from experiments using uniformly labeled glutamine. Black dots indicate labeled glutathione isotopologues (i.e., excluding glutathione m+0).
- (M) Volcano plots from correlating cysteine abundance with labeling patterns from experiments using uniformly labeled glucose. Black dots indicate labeled glutathione isotopologues (i.e., excluding glutathione m+0).

### Immune cell populations in the ccRCC TME remodel bulk tumor metabolism

When comparing the expression of various immune signatures in PC2<sub>high</sub> regions with that in PC2<sub>low</sub> regions, we found significant enrichment of T cell and macrophage cell populations in PC2<sub>high</sub> regions (Figure S4J). Based on this evidence and observations by others that immune and tumor cells compete for nutrients and signaling factors in the ccRCC microenvironment,<sup>22–27</sup> we hypothesized that the metabolome and immune microenvironment might co-evolve to produce niches with defined patterns of metabolite abundance and immune cell composition. To systematically test this hypothesis, we studied the interaction between the immune microenvironment and metabolic phenotypes using a previously validated RNA signature of generic immune infiltration (immune score) in each sample.<sup>28</sup> To control for our repeated measurements of different regions from the same patient, we used a mixed-effects model with patient as a random effect. Significance was determined by parametric bootstrapping (100,000 iterations) (Figure 4A; STAR Methods).

In total, 33/602 (5%) metabolites were significantly associated with immune score across patients (FDR-adjusted  $p < 0.05$ ) (Figure 4B). These immune-associated metabolites included both glutathione and cysteine, which were differentially abundant when comparing PC2<sub>high</sub> with PC2<sub>low</sub> regions (Figure 3C), as well as several metabolites associated with NAD<sup>+</sup> metabolism (nicotinamide, quinolinate, and 1-methyl-2-pyridone-5-carboxamide). Pathway analysis revealed that plasmalogens and NAD<sup>+</sup> metabolism pathways were enriched for immune score covariation (Figure 4C). Confirming that mixed-effects modeling capture intrapatient relationships between metabolites and immune score, the correlative relationship between metabolites and immune score was preserved intratumorally: taking nicotinamide and quinolinate as examples, regions with the highest levels of immune score expression also demonstrated higher levels of quinolinate (Wilcoxon paired  $p = 0.02$ ) and nicotinamide (Wilcoxon paired  $p = 0.03$ ) (Figure 4D). Importantly, the association between metabolite levels and immune infiltration (via immune score) was corroborated in a recently published multimodal, single-region study of ccRCC<sup>29</sup> ( $p = 1 \times 10^{-5}$ , rho = 0.53; Figure S4K). Together, these analyses suggest that the metabolome can be altered by increased immune infiltration and specific metabolites, including, but not limited to, those involved in NAD<sup>+</sup> metabolism, are strongly correlated to the extent of immune cell infiltration.

### Metabolic features of prognostic immune signatures in ccRCC

The immune score analysis above represents a crude estimation of the total immune infiltration of a tumor, summing together diverse myeloid and lymphoid cell populations with both pro- and anti-tumorigenic properties. Importantly, emerging data now indicate that RNA signatures capturing certain aspects of the ccRCC microenvironment, including angiogenic gene expression and myeloid/T-effector abundance, are associated with response to therapy in ccRCC.<sup>30–32</sup> Given the association between the tumor microenvironment (TME) and the metabolome (Figure 4B) and generically between transcript levels and metabolite levels (Figure 2), we hypothesized that these signatures may themselves also reflect distinct metabolic pheno-

types. Three different signatures, qualitatively reflecting the abundance of cytotoxic ("JAVELIN")<sup>32</sup> cells and myeloid ("Myeloid")<sup>30</sup> cells, and the activity of angiogenesis ("Angiogenesis")<sup>30</sup> in the tumor, have been identified through retrospective analysis of response data in several clinical trials of immunotherapy and/or anti-VEGF therapy in ccRCC. We confirmed that the expression levels of these signatures were significantly correlated to immunofluorescence staining (angiogenesis signature/CD31, rho = 0.63,  $p = 3 \times 10^{-4}$ , Figure 5A; myeloid signature/CD68, rho = 0.58,  $p = 0.001$ , Figure 5B). Representative images of immunofluorescence staining are in Figure 5C.

We again used mixed-effects models to identify metabolites associated with the angiogenesis, myeloid, and JAVELIN scores. There was substantial variability in the association between metabolite levels and prognostic RNA signatures. In total, we identified no metabolites associated with the JAVELIN signature (Figure 5D) and 4 metabolites significantly associated with the angiogenesis signature (Figure 5E). In contrast, 47/602 metabolites (8% of the measured metabolome) were associated with the myeloid signature (Figure 5F). The myeloid signature has been associated with inferior outcomes in patients treated with systemic therapy and with recurrence in high-risk localized disease.<sup>33,34</sup> Metabolites associated with myeloid infiltration concentrated into certain pathways, including most prominently n-acetylated amino acids (NAAs, including n-acetylarginine, n-acetylasparagine, n-acetylglutamine, n-acetylleucine, n-acetylalanine, n-acetylaspartate, and n-acetylmethionine). Most notably, the immunomodulatory metabolite kynurenine,<sup>35,36</sup> which was the target of recent negative clinical trials of inhibitors of its upstream enzyme *IDO1* (which is significantly positively associated with kynurenine,  $p < 2.2 \times 10^{-16}$ ), was significantly negatively associated with the myeloid signature (FDR-adjusted  $p = 5 \times 10^{-3}$ ). These findings indicate that the presence of myeloid cells in the immune microenvironment is strongly associated with a unique pattern of metabolite abundance.

Next, we more granularly investigated the specific myeloid cell populations exhibiting strong correlation with NAA abundance using RNA-based signatures for mast cells, dendritic cells, neutrophils, and macrophages. This analysis revealed that dendritic cells and macrophages were significantly associated with 71/602 (12%) and 80/602 (13%) of metabolites, including several NAAs, respectively (Figures 5G and 5H). To identify the putative cellular source of NAAs, we first investigated the association between NAAs and the expression of N-acetyltransferase genes acting on them, which identified two genes *NAT8* and *NAT8B*, which exhibited strong and broad correlation to numerous NAAs (Figure 5I). To understand the microenvironmental cellular source driving NAA levels, we used single-cell RCC data to evaluate the cell-type-specific expression of *NAT8/NAT8B* across cell types. Whereas *NAT8B* was not abundantly expressed, we found that *NAT8* expression was highest in tumor and kidney epithelial cells, potentially implying that epithelial, rather than myeloid, cells drove NAA abundance (Figure 5J). We further reasoned that, if myeloid cells did, indeed, drive the variation in NAA abundance, then the correlation between myeloid cell infiltration and NAA abundance would be preserved in adjacent normal kidney tissue. However, when tested, no significant association between myeloid infiltration and NAA abundance was found in normal kidney. From these analyses, we concluded

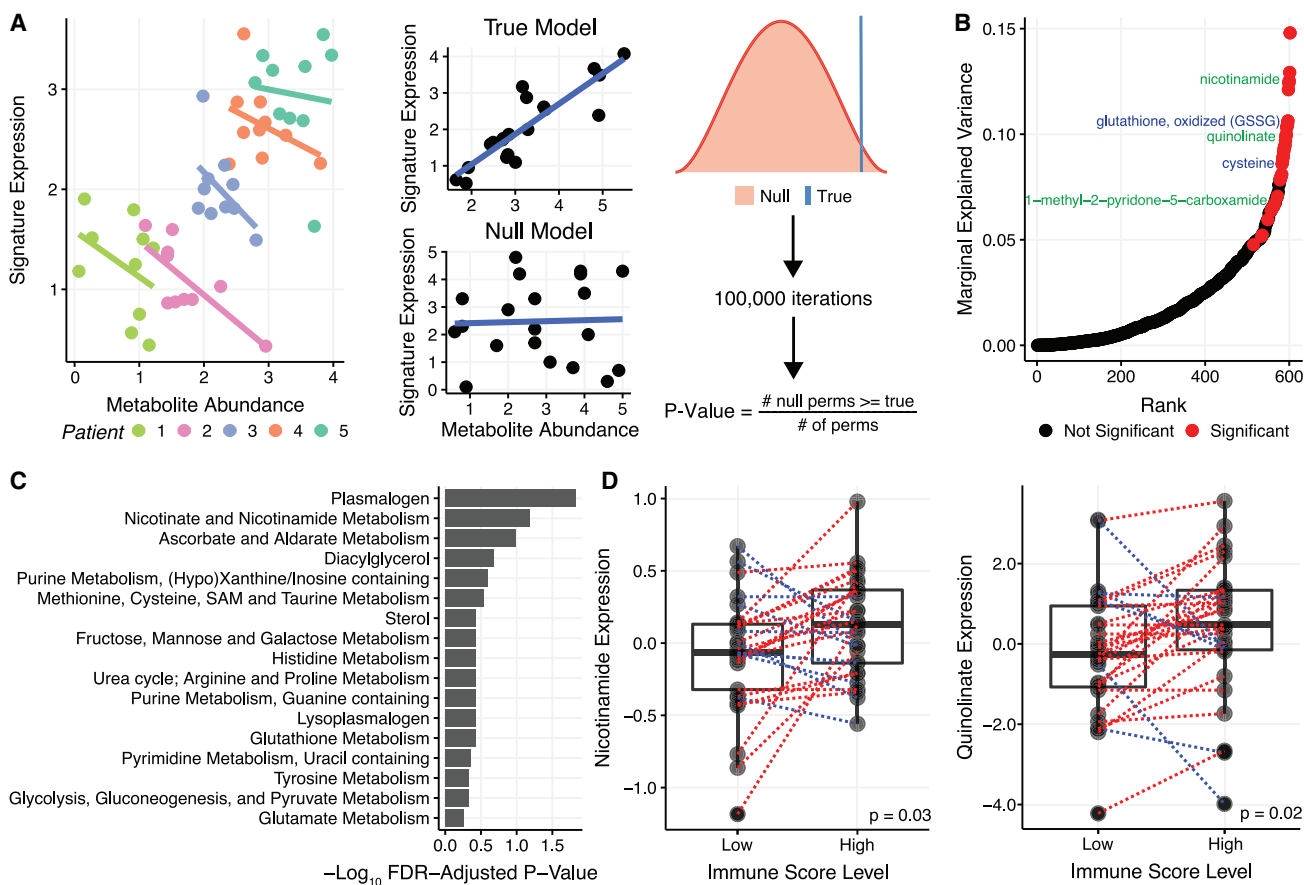


**Figure 4. Immune infiltration in ccRCC tumors is associated with unique metabolomic profiles**

(A) Left: scatterplot illustrating Simpson's paradox, where non-independence in data due to a patient-level random effect, confounds the co-expression pattern between two variables. Right: in parametric bootstrapping, the true model is compared with the null model where the p value is the fraction of times the null model test statistic from the null model is at least as extreme as the true test statistic. In total, 100,000 bootstraps were performed.

(B) Marginal explained variance in a mixed-effects linear model of metabolite levels predicting immune score with patient added as a random effect. Each dot represents a single metabolite. Significant metabolites in the NAD<sup>+</sup> metabolism pathway are labeled in green, whereas significant metabolites in the glutathione pathway are labeled in blue.

(C) Fisher's exact test was performed on pathways with 3+ metabolites to determine pathways with a significantly higher proportion of their metabolites associated with immune score based on the mixed-effects model. The barplot shows FDR-adjusted p values from Fisher's exact test.

(D) Nicotinamide and quinolinolate levels are elevated in tumor regions with high immune infiltration relative to paired tumor regions with low immune infiltration.

that the association between myeloid and NAAs most likely arose from a tumor-cell-intrinsic modulation of the expression of N-acetyltransferase genes in the presence of myeloid cells in the TME.

#### Machine learning predicts the metabolic profiles of response to the tyrosine kinase inhibitor sunitinib

Based on the association between metabolite levels and the prognostically significant myeloid signature, we hypothesized that certain metabolomic profiles may directly associate with patients' response to anti-angiogenic or immune checkpoint blockade therapy. However, the identification of the metabolic biomarkers of response to therapy has historically been limited because of the scarcity of metabolomics data themselves, which rely on significant quantities of fresh frozen tumor tissue. Premised on the strong association between transcript and metabolite levels in Figure 4A, we hypothesized that the abundance of a subset of metabolites could be imputed from transcriptomics

data (in a manner similar to RNA signatures and immune deconvolution). To evaluate this possibility, we applied a previously published machine learning algorithm (MIRTH) developed by our group.<sup>37</sup> In this context, MIRTH imputes unmeasured metabolites in a target dataset by learning the relationship between RNA and metabolite levels in a reference dataset where both RNA and metabolites are measured (Figure S5; STAR Methods).

We first sought to benchmark whether MIRTH could impute biologically reasonable metabolic phenotypes. To do so, we utilized three batches of in-house ccRCC samples with matched RNA and metabolomics data (including both M4 and M5 datasets and an additional M1 dataset related to a prior publication<sup>1</sup>) as reference datasets and the TCGA ccRCC cohort (for which only RNA data were available) as the target dataset for imputation. We then applied MIRTH to impute 606 tumor and adjacent normal samples from TCGA. Imputed metabolite levels in the TCGA preserved ground-truth differences between both tumor/normal samples (Spearman's rho = 0.85, p = 1.6 × 10<sup>-31</sup>)

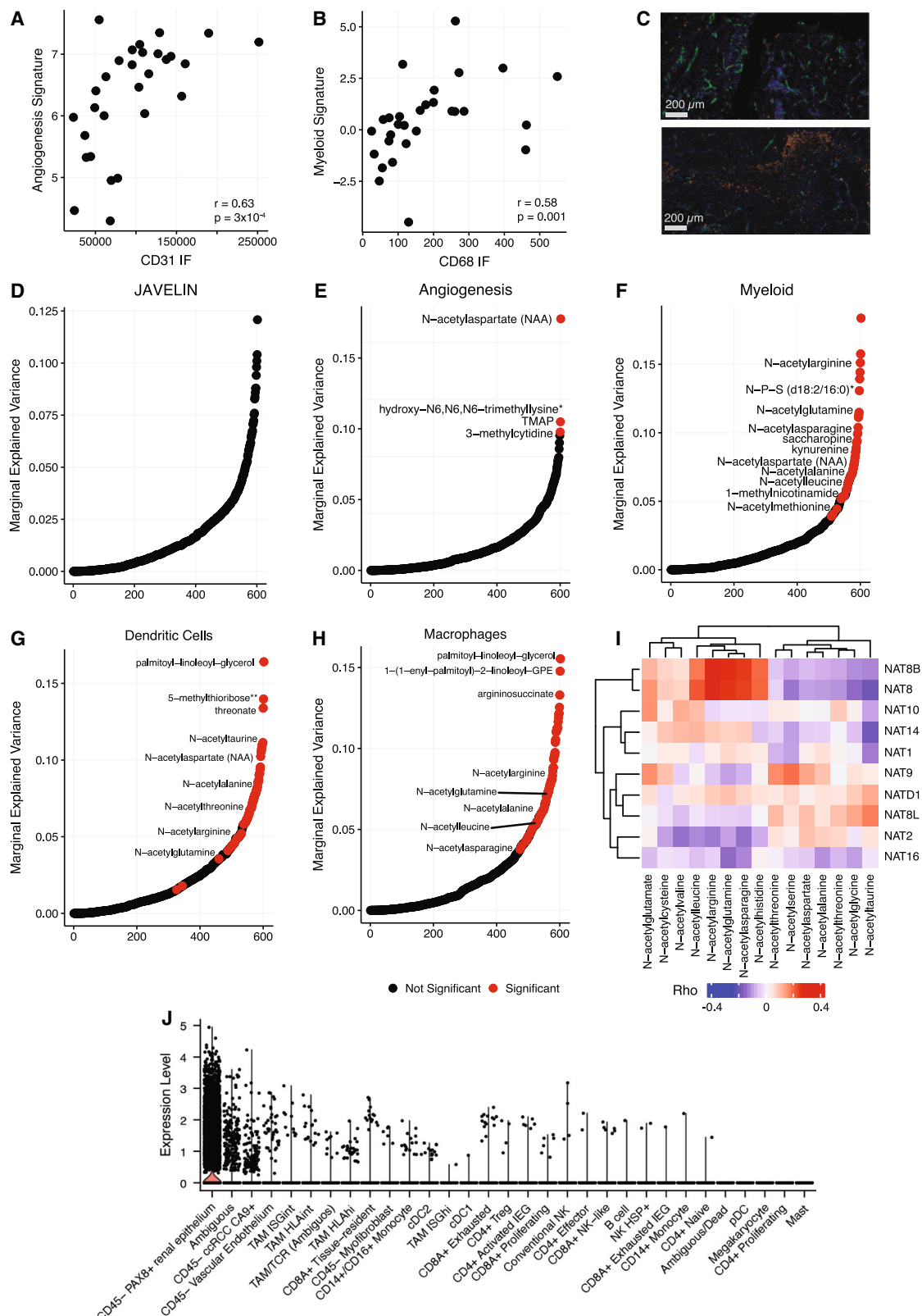


**Figure 5. Metabolic features of prognostic immune signatures in ccRCC**

(A) Scatterplot comparing CD31 levels from IF staining to the expression levels of the McDermott angiogenesis signature.  
(B) Scatterplot comparing CD68 levels from IF staining to the expression levels of the McDermott myeloid signature.

(legend continued on next page)

and high-stage/low-stage samples (Spearman's rho = 0.39, p =  $3.0 \times 10^{-5}$ ) (Figure 6A). To further ascertain the accuracy of MIRTH in imputing metabolite levels from RNA data, we benchmarked it on a large dataset of over 900 cancer cell lines jointly profiled by RNA sequencing and metabolomic sequencing in the CCLE. By artificially partitioning the CCLE data into a reference dataset (50% of all cell lines, matched RNA/metabolite data) and a target dataset (50% of all cell lines, RNA data only), we found that MIRTH accurately imputed 96% of metabolites (FDR-corrected Spearman p < 0.05 and Spearman's rho > 0.3) (Figure 6B). Immunomodulatory metabolites, such as 1-methylnicotinamide, were imputed with exceptionally high accuracy (Figure 6C). Together, these data establish the value of MIRTH as a tool for imputing otherwise unmeasured metabolite levels in a diverse set of diseases beyond ccRCC data (Figure 6B). Altogether, these data establish that MIRTH successfully imputes metabolite levels from RNA sequencing data across diverse cancer types in solid tumors and cell lines, preserves metabolic relationships between subsets of tumor/normal samples, and learns signatures of progression to aggressive disease.

We then applied MIRTH to impute metabolite levels from RNA sequencing data from 7 publicly available advanced ccRCC clinical trials where patients were treated with either immunotherapy (in combination or alone) or sunitinib (a tyrosine kinase inhibitor, typically used in the control arm of these trials). For 262 metabolites with accurate imputation on cross-validation, we verified that MIRTH imputation preserved the correlative relationship between metabolites and the immune score signature relative to data from M4/M5 (Figure S5D). Next, we evaluated the association between each of the 262 well-predicted metabolites and progression-free survival (PFS) by multivariate Cox proportional hazards models (evaluating different treatment arms separately.) The number of metabolites associated with response varied across each trial and arm, motivating us to identify metabolites with consistent patterns across the trials. Meta-analysis results across 7 clinical trials identified 7 metabolites significantly associated with improved PFS in the sunitinib arms (FDR-adjusted p < 0.05) (Figure 6D) and no metabolites significantly associated with PFS in immunotherapy treatment arms (Figure S5E). Among the metabolites associated with sunitinib were saccharopine and N-palmitoyl-sphingadienine (d18:2/16:0), which were also significantly associated with the myeloid signature (Figure 5F). The strongest association with sunitinib response was observed in patients with high 1-methylimidazoleacetate (Figure 6E). 1-methylimidazoleacetate is a catabolite of the inflammation-mediating metabolite histamine, suggesting that local inflammation in the tumor may in part mediate response to sunitinib.<sup>38</sup> Thus, by training a model to impute metabolite levels from transcriptomic data, MIRTH enables the identification of otherwise cryptic metabolite biomarkers in publicly available trial data.

## DISCUSSION

The intratumoral genotypic and phenotypic diversification of ccRCC tumors<sup>2,39</sup> influences future tumor evolution and likely shapes the development of metastasis and response to therapy.<sup>40–47</sup> Motivated by the numerous studies implicating remodeled metabolism as a hallmark of ccRCC tumorigenesis and progression, we investigated how IMH manifests and studied the underlying genetic, transcriptomic, and microenvironmental factors driving metabolic diversification. Using multiregional sampling of the metabolome, genome, and transcriptome, we identified a metabolic program that compensates for ferroptotic susceptibility and drives a substantial fraction of total IMH. Transcriptomic factors, reflecting in part the cellular composition of the TME, influenced metabolomic variation within tumors more than genetic factors. In turn, a large fraction of the metabolome was correlated both to the extent of generic immune infiltration in the tumor and, more specifically, to the abundance of myeloid cells in the TME. Seizing on the association between the transcriptome and metabolome, we applied a machine learning algorithm (MIRTH) to impute metabolite levels from RNA sequencing data and identified a set of metabolites that were reproducibly associated with response to anti-VEGF therapy in ccRCC patients. Importantly, MIRTH naturally generalizes to other cancer types (Figure 6B) and diseases with paired metabolomics and transcriptomics data and can, therefore, be used to democratize metabolomic data analysis in contexts where the availability of fresh frozen primary tissue for metabolomics is limited. MIRTH is thus a means for the discovery of new metabolomic biomarkers and/or targets for therapeutic intervention.

Recent functional data suggest that stochastic heterogeneity in the metabolic phenotypes of tumor cells can endow a subset of cells with the capacity to metastasize.<sup>9,10</sup> Complementing these data, our group and others have shown that the abundance of glutathione and its related metabolites is associated with metastatic disease and the risk of recurrence in ccRCC.<sup>1</sup> Here, we discovered that all ccRCC tumors evolve along a common axis of IMH that produces spatially delimited tumor regions defined by the elevation of metabolites associated with glutathione and its related precursors (e.g., cysteine). These data motivate a new model whereby the metabolic diversification of ccRCC ultimately produces tumor subclones with elevated glutathione levels that can ultimately seed distant metastases. Importantly, identifying the selective pressures placed on metabolism in metastases will likely require multimodal data and integrative analysis to reconcile apparently conflicting data: although a comparison of transcriptional phenotypes of metastatic and primary tissues from the ImMotion151 phase III clinical trial reveals no difference in the expression of OXPHOS genes between primary and metastatic tissues (mean difference = 69.9, p = 0.055), recent direct measurements of metabolic flux

(C) Top: representative IF image of a tumor region (MR01\_RB) with high CD31 expression (green) and low CD68 expression (orange). Bottom: representative IF image of a tumor region (MR01\_RE) with low CD31 expression and high CD68 expression. Scale bar represents 200  $\mu$ m.

(D–H) Marginal explained variance in a mixed-effects linear model of metabolite levels predicting JAVELIN (D), McDermott angiogenesis (E), McDermott myeloid (F), dendritic cell (G), and macrophage (H) signature expression with patient added as a random effect. Each dot represents a single metabolite. Red dots indicate statistically significant associations.

(I) Heatmap Spearman correlation coefficients between NAT genes and n-acetylated amino acids.

(J) Boxplots of NAT8 expression levels across cell types in a single-cell RNA sequencing ccRCC dataset.

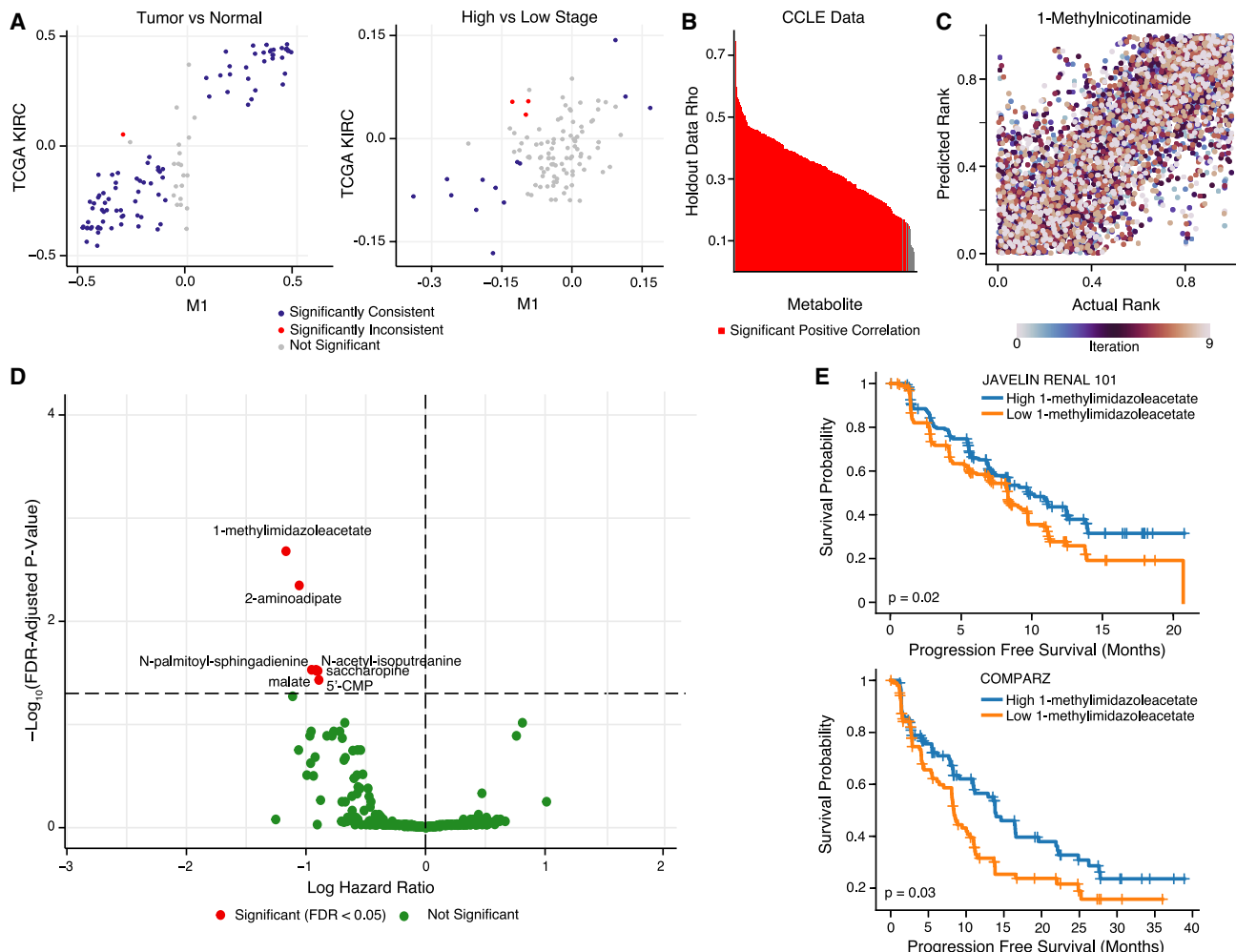


**Figure 6. Metabolic profiles of response to sunitinib predicted by MIRTH**

(A) Scatterplot comparing the differential abundance of imputed metabolites in TCGA KIRC to ground-truth in M1. Comparison is between tumor vs. normal samples (left) and high-stage vs. low-stage samples (right). Metabolites in blue are consistently and significantly differentially enriched (FDR-adjusted  $p < 0.05$  and rank difference  $> 0$  or  $< 0$  in both datasets, Wilcoxon rank-sum test). Metabolites in red are discrepant between imputed and ground-truth data.

(B) Barplot of median Spearman's correlation values for each simulated missing metabolite in CCLE data across 10 MIRTH iterations. Metabolites whose predicted ranks are significantly positively correlated with ground-truth ranks in  $>90\%$  of iterations are labeled red.

(C) Scatterplot of actual vs. predicted ranks for 1-methylnicotinamide in CCLE data. Dots are colored by iteration.

(D) Volcano plot of hazard ratios relating 262 reproducibly well-imputed metabolites to PFS in sunitinib arms of ccRCC clinical trials, colored by significance (Cox's proportional hazards test, adjusted by age and sex). Metabolites in red are significant (FDR-adjusted  $p < 0.05$ ). x axis is in natural log space.

(E) Kaplan-Meier plot showing that sunitinib-treated ccRCC patients with a high level of 1-methylimidazole acetate (based on median level of 1-methylimidazole acetate) had improved PFS than patients with low level of 1-methylimidazole acetate in the JAVELIN RENAL 101 (top) and COMPARZ (bottom) trials.

suggest that ccRCC metastases may increase their respiratory capacity relative to primary tumors.

Among the most significant, but also comparatively provocative, limitations of this and other metabolomic studies of primary tumors is that the measurements of the tumor metabolome are nearly always taken in bulk and, therefore, represent a complex mixture of metabolite signals from the constituent tumor and non-tumor (immune and stromal) cells in the microenvironment. Our data here suggest that the cellular composition of the immune microenvironment is associated with specific metabolomic features and complements newly emerging data on the partitioning of nutrient consumption across cellular compartments.<sup>23</sup> The

coevolution of the tumor metabolome and immune microenvironment likely arises from a combination of several phenomena: (1) cell-type-specific accumulation/depletion of specific metabolites (such as those previously described for 1-methylnicotinamide in ovarian cancer<sup>24</sup>); (2) competition among different cell populations for nutrients in the circulation<sup>48</sup>, and (3) systemic features of the metabolism of the patient, including, but not limited to, factors such as obesity and metabolic syndrome.<sup>49,50</sup> There is ample evidence of metabolite-level effects on immune response, including the downregulation of glycolysis by CTLA-4 in T cells,<sup>25</sup> the inhibition of T cell proliferation by the expression of 2,3-dioxygenase in tumor cells,<sup>48</sup> and the suppression of T cell function by

tumor-derived lactate secretion.<sup>48</sup> In support of these findings, large-scale analysis of public clinical trial data here (Figure 6) suggests that the abundance of a subset of metabolites in primary tumor tissue may be associated with response to approved therapies in ccRCC. These discoveries may provide a means for stratifying patients according to their likelihood to respond to metabolically targeted therapies (e.g., IDO1/epacadostat<sup>51</sup>). Our findings, in combination with these prior discoveries, suggest that therapeutic strategies that rationally target the metabolome and immune microenvironment in combination may improve response to therapy in ccRCC.

### Limitations of study

Several limitations must be considered when interpreting the conclusions of our study. Due to the multiregional nature of our study, the sample size in terms of patients is relatively small, and statistical power is further diluted by the separation of metabolomic profiling into two batches. Such sample size limitations may soon be overcome as spatial metabolomic technologies capable of sampling intratumoral heterogeneity at significantly higher resolution become more widely adopted. Although we validated several RNA signatures of immune cell infiltration with matched immunofluorescence data, caution must nevertheless be taken in interpreting the covariation of RNA-based signatures of immune infiltration and metabolite levels. More robust signatures, learned from newly abundant single-cell sequencing data, may potentially overcome this challenge. Finally, the causal source of covariation between the metabolome and the immune microenvironment remains unclear. Further mechanistic experiments are required to evaluate whether certain metabolic milieus are caused by or may engender the development of immune microenvironments with defined cellular composition.

### STAR★METHODS

Detailed methods are provided in the online version of this paper and include the following:

- **KEY RESOURCES TABLE**
- **RESOURCE AVAILABILITY**
  - Lead contact
  - Materials availability
  - Data and code availability
- **EXPERIMENTAL MODEL AND SUBJECT DETAILS**
  - Tumor sampling
- **METHOD DETAILS**
  - Sample preparation and metabolomic profiling
  - Data normalization
  - Necrosis pathology review
  - Whole transcriptome sequencing
  - RNA-seq data processing pipeline
  - Whole-exome sequencing
  - WES data processing pipeline
  - Bulk RNA-seq deconvolution analysis
  - Bulk gene set enrichment analysis
  - Metabolomics and RNA ITH scores
  - DNA ITH scores
  - Differential abundance score

- Robinson-Foulds distance
- GPX4 immunohistochemistry
- Linear mixed modelling of immune phenotypes
- Immunofluorescence for CD31 and CD68
- Imputation of metabolites by RNA with MIRTH
- Survival analysis

### ● QUANTIFICATION AND STATISTICAL ANALYSIS

- Statistical analysis

### ● ADDITIONAL RESOURCES

### SUPPLEMENTAL INFORMATION

Supplemental information can be found online at <https://doi.org/10.1016/j.cmet.2023.06.005>.

### ACKNOWLEDGMENTS

We thank Sohrab Shah, Kayvan Keshari, and Jan Krumsiek for their thoughtful feedback. Graphics were created with [www.BioRender.com](http://www.BioRender.com). E.R. was supported by the Geoffrey Beene Cancer Research Center Grant Award, Department of Defense Kidney Cancer Research Program (no. W81XWH-18-1-0318), Cycle For Survival Equinox Innovation Award, Kidney Cancer Association Young Investigator Award, Brown Performance Group Innovation in Cancer Informatics Fund, and NIH R37 CA276200. A.A.H. was supported by NIH R01 CA258886, DOD KCRP grant W81XWH-21-1-0941, the Mazumdar-Shaw Kidney Cancer Fund, and the Weiss Family Fund. E.R. and A.A.H. were jointly supported by a grant from the Alan and Sandra Gerry Metastasis and Tumor Ecosystems Center. This work was supported by NIH/NCI Cancer Center Support Grant (P30 CA008748).

### AUTHOR CONTRIBUTIONS

C.T., E.R., and A.A.H. designed the study, analyzed the data, and drafted the manuscript. A.X.X. and F.K. analyzed the data and edited the manuscript. M.K. edited the manuscript. R.G.D. and M.G. analyzed the data. Y.-B.C. and S.G. performed the pathologic analysis and edited the manuscript. R.J.M., P.R., J.C., M.I.C., M.H.V., R.R.K., and C.-H.L. provided surgical samples and edited the manuscript. W.T. analyzed the data and developed the MIRTH algorithm. N.S., A.A.H., and E.R. supervised the study.

### DECLARATION OF INTERESTS

R.R.K. is a consultant and/or on the Advisory Board of Eisai and reports receiving institutional research funding from Pfizer, Takeda, Novartis, Xencor, and Allogene Therapeutics. Y.-B.C. is a consultant for InspiRNA, Inc. M.H.V. is a consultant and/or on the Advisory Board of Eisai, Exelixis, Merck, Calithera, Aveo, Genentech, Oncorena, Affimed, MICU Rx Aravive, onQuality, AstraZeneca, and Mertelsmann Foundation. M.H.V. has received research funding from Pfizer, BMS, and Genentech. C.-H.L. has received research funding from AstraZeneca, BMS, Calithera, Eisai, Eli Lilly, Exelixis, and Merck. C.-H.L. is a consultant for Aadi, Aveo, BMS, Exelixis, Eisai, Merck, Pfizer, EMD Serono, and Cardinal Health. C.-H.L. has received honoraria from AiCME, IDEOlogy Health, Intellisphere, Medscape, MJH, and Research to Practice. M.G. was an employee and a shareholder of Illumina Inc. during the preparation of this study. M.G. is currently an employee and a shareholder of Roche. R.J.M. is a consultant and/or on the Advisory Board of AstraZeneca, Aveo, Calithera Biosciences, Eisai, Exelixis, Genentech/Roche, Incyte, Pfizer, and Merck. R.J.M. has received research funding from Aveo, Bristol Myers Squibb, Eisai, Exelixis, Genentech/Roche, Novartis, Pfizer, and Merck. A.A.H. is on the Advisory Board of Merck. E.R. is a consultant for Xontogeny, LLC.

Received: October 12, 2022

Revised: March 10, 2023

Accepted: June 6, 2023

Published: July 5, 2023

### REFERENCES

- Hakimi, A.A., Reznik, E., Lee, C.-H., Creighton, C.J., Brannon, A.R., Luna, A., Aksoy, B.A., Liu, E.M., Shen, R., Lee, W., et al. (2016). An integrated metabolic atlas of clear cell renal cell carcinoma. *Cancer Cell* 29, 104–116. <https://doi.org/10.1016/j.ccr.2015.12.004>.
- Gerlinger, M., Rowan, A.J., Horswell, S., Math, M., Larkin, J., Endesfelder, D., Gronroos, E., Martinez, P., Matthews, N., Stewart, A., et al. (2012). Intratumor heterogeneity and branched evolution revealed by multiregion sequencing. *N. Engl. J. Med.* 366, 883–892. <https://doi.org/10.1056/NEJMoa113205>.
- Şenbabaoğlu, Y., Gejman, R.S., Winer, A.G., Liu, M., Van Allen, E.M., de Velasco, G., Miao, D., Ostrovnyaya, I., Drill, E., Luna, A., et al. (2016). Tumor immune microenvironment characterization in clear cell renal cell carcinoma identifies prognostic and immunotherapeutically relevant messenger RNA signatures. *Genome Biol.* 17, 231. <https://doi.org/10.1186/s13059-016-1092-z>.
- Reznik, E., Luna, A., Aksoy, B.A., Liu, E.M., La, K., Ostrovnyaya, I., Creighton, C.J., Hakimi, A.A., and Sander, C. (2018). A landscape of metabolic variation across tumor types. *Cell Syst.* 6, 301–313.e3. <https://doi.org/10.1016/j.cels.2017.12.014>.
- Cancer; Genome; Atlas; Research Network (2013). Comprehensive molecular characterization of clear cell renal cell carcinoma. *Nature* 499, 43–49. <https://doi.org/10.1038/nature12222>.
- Li, B., Qiu, B., Lee, D.S.M., Walton, Z.E., Ochocki, J.D., Mathew, L.K., Mancuso, A., Gade, T.P.F., Keith, B., Nissim, I., and Simon, M.C. (2014). Fructose-1,6-bisphosphatase opposes renal carcinoma progression. *Nature* 513, 251–255. <https://doi.org/10.1038/nature13557>.
- Jing, L., Guigonis, J.-M., Borchiellini, D., Durand, M., Pourcher, T., and Ambrosetti, D. (2019). LC-MS based metabolomic profiling for renal cell carcinoma histologic subtypes. *Sci. Rep.* 9, 15635. <https://doi.org/10.1038/s41598-019-52059-y>.
- Reigle, J., Secic, D., Biesiada, J., Wetzel, C., Shamsaei, B., Chu, J., Zang, Y., Zhang, X., Talbot, N.J., Bischoff, M.E., et al. (2021). Tobacco smoking induces metabolic reprogramming of renal cell carcinoma. *J. Clin. Invest.* 131, e140522. <https://doi.org/10.1172/JCI140522>.
- Rossi, M., Altea-Manzano, P., Demicco, M., Doglioni, G., Bornes, L., Fukano, M., Vandekere, A., Cuadros, A.M., Fernández-García, J., Riera-Domingo, C., et al. (2022). PHGDH heterogeneity potentiates cancer cell dissemination and metastasis. *Nature* 605, 747–753. <https://doi.org/10.1038/s41586-022-04758-2>.
- Tasdogan, A., Faubert, B., Ramesh, V., Ubellacker, J.M., Shen, B., Solmonson, A., Murphy, M.M., Gu, Z., Gu, W., Martin, M., et al. (2020). Metabolic heterogeneity confers differences in melanoma metastatic potential. *Nature* 577, 115–120. <https://doi.org/10.1038/s41586-019-1847-2>.
- Okegawa, T., Morimoto, M., Nishizawa, S., Kitazawa, S., Honda, K., Araki, H., Tamura, T., Ando, A., Satomi, Y., Nutahara, K., and Hara, T. (2017). Intratumor heterogeneity in primary kidney cancer revealed by metabolic profiling of multiple spatially separated samples within tumors. *EBioMedicine* 19, 31–38. <https://doi.org/10.1016/j.ebiom.2017.04.009>.
- Zhang, Y., Udayakumar, D., Cai, L., Hu, Z., Kapur, P., Kho, E.-Y., Pavía-Jiménez, A., Fulkerson, M., de Leon, A.D., Yuan, Q., et al. (2017). Addressing metabolic heterogeneity in clear cell renal cell carcinoma with quantitative Dixon MRI. *JCI Insight* 2, e94278. <https://doi.org/10.1172/jci.insight.94278>.
- Miao, D., Margolis, C.A., Gao, W., Voss, M.H., Li, W., Martini, D.J., Norton, C., Bossé, D., Wankowicz, S.M., Cullen, D., et al. (2018). Genomic correlates of response to immune checkpoint therapies in clear cell renal cell carcinoma. *Science* 359, 801–806. <https://doi.org/10.1126/science.aan5951>.
- Biswas, D., Birkbak, N.J., Rosenthal, R., Hiley, C.T., Lim, E.L., Papp, K., Boeing, S., Krzystanek, M., Djureinovic, D., La Fleur, L., et al. (2019). A clonal expression biomarker associates with lung cancer mortality. *Nat. Med.* 25, 1540–1548. <https://doi.org/10.1038/s41591-019-0595-z>.
- Green, D.R., Galluzzi, L., and Kroemer, G. (2014). Cell biology. Metabolic control of cell death. *Science* 345, 1250256. <https://doi.org/10.1126/science.1250256>.
- Ogretmen, B. (2018). Sphingolipid metabolism in cancer signalling and therapy. *Nat. Rev. Cancer* 18, 33–50. <https://doi.org/10.1038/nrc.2017.96>.
- Jiang, X., Stockwell, B.R., and Conrad, M. (2021). Ferroptosis: Mechanisms, biology and role in disease. *Nat. Rev. Mol. Cell Biol.* 22, 266–282. <https://doi.org/10.1038/s41580-020-00324-8>.
- Dixon, S.J., Lemberg, K.M., Lamprecht, M.R., Skouta, R., Zaitsev, E.M., Gleason, C.E., Patel, D.N., Bauer, A.J., Cantley, A.M., Yang, W.S., et al. (2012). Ferroptosis: An iron-dependent form of nonapoptotic cell death. *Cell* 149, 1060–1072. <https://doi.org/10.1016/j.cell.2012.03.042>.
- Zhang, L., Hobeika, C.S., Khabibullin, D., Yu, D., Filippakis, H., Alchoueiry, M., Tang, Y., Lam, H.C., Tsvetkov, P., Georgiou, G., et al. (2022). Hypersensitivity to ferroptosis in chromophobe RCC is mediated by a glutathione metabolic dependency and cystine import via solute carrier family 7 member 11. *Proc. Natl. Acad. Sci. USA* 119, e2122840119. <https://doi.org/10.1073/pnas.2122840119>.
- Zou, Y., Palte, M.J., Deik, A.A., Li, H., Eaton, J.K., Wang, W., Tseng, Y.-Y., Deasy, R., Kost-Alimova, M., Dančík, V., et al. (2019). A GPX4-dependent cancer cell state underlies the clear-cell morphology and confers sensitivity to ferroptosis. *Nat. Commun.* 10, 1617. <https://doi.org/10.1038/s41467-019-10927-9>.
- Wang, L., Xing, X., Zeng, X., Jackson, S.R., TeSlaa, T., Al-Dalahmah, O., Samarah, L.Z., Goodwin, K., Yang, L., McReynolds, M.R., et al. (2022). Spatially resolved isotope tracing reveals tissue metabolic activity. *Nat. Methods* 19, 223–230. <https://doi.org/10.1038/s41592-021-01378-y>.
- Lau, A.N., and Vander Heiden, M.G. (2020). Metabolism in the tumor microenvironment. *Annu. Rev. Cancer Biol.* 4, 17–40. <https://doi.org/10.1146/annurev-cancerbio-030419-033333>.
- Reinfeld, B.I., Madden, M.Z., Wolf, M.M., Chytil, A., Bader, J.E., Patterson, A.R., Sugiura, A., Cohen, A.S., Ali, A., Do, B.T., et al. (2021). Cell-programmed nutrient partitioning in the tumour microenvironment. *Nature* 593, 282–288. <https://doi.org/10.1038/s41586-021-03442-1>.
- Kilgour, M.K., MacPherson, S., Zacharias, L.G., Ellis, A.E., Sheldon, R.D., Liu, E.Y., Keyes, S., Pauly, B., Carleton, G., Allard, B., et al. (2021). 1-methylnicotinamide is an immune regulatory metabolite in human ovarian cancer. *Sci. Adv.* 7, eabe1174. <https://doi.org/10.1126/sciadv.abe1174>.
- Zappasodi, R., Srganova, I., Cohen, I.J., Maeda, M., Shindo, M., Senbabaoğlu, Y., Watson, M.J., Leftin, A., Maniyar, R., Verma, S., et al. (2021). CTLA-4 blockade drives loss of Treg stability in glycolysis-low tumors. *Nature* 591, 652–658. <https://doi.org/10.1038/s41586-021-03326-4>.
- Moffett, J.R., Arun, P., Puthillathu, N., Vengilote, R., Ives, J.A., Badawy, A.A.-B., and Namboodiri, A.M. (2020). Quinolinate as a marker for kynurene metabolite formation and the unresolved question of NAD<sup>+</sup> synthesis during inflammation and infection. *Front. Immunol.* 11, 31. <https://doi.org/10.3389/fimmu.2020.00031>.
- Cascone, T., McKenzie, J.A., Mbofung, R.M., Punt, S., Wang, Z., Xu, C., Williams, L.J., Wang, Z., Bristow, C.A., Carugo, A., et al. (2018). Increased tumor glycolysis characterizes immune resistance to adoptive T cell therapy. *Cell Metab.* 27, 977–987.e4. <https://doi.org/10.1016/j.cmet.2018.02.024>.
- Yoshihara, K., Shahmoradgoli, M., Martínez, E., Vegesna, R., Kim, H., Torres-Garcia, W., Treviño, V., Shen, H., Laird, P.W., Levine, D.A., et al. (2013). Inferring tumor purity and stromal and immune cell admixture from expression data. *Nat. Commun.* 4, 2612. <https://doi.org/10.1038/ncomms3612>.
- Li, Y., Lih, T.-S.M., Dhanasekaran, S.M., Mannan, R., Chen, L., Cieslik, M., Wu, Y., Lu, R.J.-H., Clark, D.J., Kołodziejczak, I., et al. (2023). Histopathologic and proteogenomic heterogeneity reveals features of clear cell renal cell carcinoma aggressiveness. *Cancer Cell* 41, 139–163.e17. <https://doi.org/10.1016/j.ccr.2022.12.001>.
- McDermott, D.F., Huseni, M.A., Atkins, M.B., Motzer, R.J., Rini, B.I., Escudier, B., Fong, L., Joseph, R.W., Pal, S.K., Reeves, J.A., et al.

- (2018). Clinical activity and molecular correlates of response to atezolizumab alone or in combination with bevacizumab versus sunitinib in renal cell carcinoma. *Nat. Med.* 24, 749–757. <https://doi.org/10.1038/s41591-018-0053-3>.
31. Masiero, M., Simões, F.C., Han, H.D., Snell, C., Peterkin, T., Bridges, E., Mangala, L.S., Wu, S.Y.-Y., Pradeep, S., Li, D., et al. (2013). A core human primary tumor angiogenesis signature identifies the endothelial orphan receptor ELTD1 as a key regulator of angiogenesis. *Cancer Cell* 24, 229–241. <https://doi.org/10.1016/j.ccr.2013.06.004>.
  32. Motzer, R.J., Robbins, P.B., Powles, T., Albiges, L., Haanen, J.B., Larkin, J., Mu, X.J., Ching, K.A., Uemura, M., Pal, S.K., et al. (2020). Avelumab plus axitinib versus sunitinib in advanced renal cell carcinoma: Biomarker analysis of the phase 3 JAVELIN Renal 101 trial. *Nat. Med.* 26, 1733–1741. <https://doi.org/10.1038/s41591-020-1044-8>.
  33. Hakimi, A.A., Voss, M.H., Kuo, F., Sanchez, A., Liu, M., Nixon, B.G., Vuong, L., Ostrovnaya, I., Chen, Y.-B., Reuter, V., et al. (2019). Transcriptomic profiling of the tumor microenvironment reveals distinct subgroups of clear cell renal cell cancer: Data from a randomized Phase III trial. *Cancer Discov.* 9, 510–525. <https://doi.org/10.1158/2159-8290.CD-18-0957>.
  34. Rappold, P.M., Vuong, L., Leibold, J., Chakiryan, N.H., Curry, M., Kuo, F., Sabio, E., Jiang, H., Nixon, B.G., Liu, M., et al. (2022). A targetable myeloid inflammatory state governs disease recurrence in clear-cell renal cell carcinoma. *Cancer Discov.* 12, 2308–2329. <https://doi.org/10.1158/2159-8290.CD-21-0925>.
  35. Capece, L., Lewis-Ballester, A., Martí, M.A., Estrin, D.A., and Yeh, S.-R. (2011). Molecular basis for the substrate stereoselectivity in tryptophan dioxygenase. *Biochemistry* 50, 10910–10918. <https://doi.org/10.1021/bi201439m>.
  36. King, N.J.C., and Thomas, S.R. (2007). Molecules in focus: Indoleamine 2,3-dioxygenase. *Int. J. Biochem. Cell Biol.* 39, 2167–2172. <https://doi.org/10.1016/j.biocel.2007.01.004>.
  37. Freeman, B.A., Jaro, S., Park, T., Keene, S., Tansey, W., and Reznik, E. (2022). MIRTH: Metabolite imputation via rank-transformation and harmonization. *Genome Biol.* 23, 184. <https://doi.org/10.1186/s13059-022-02738-3>.
  38. Branco, A.C.C.C., Yoshikawa, F.S.Y., Pietrobon, A.J., and Sato, M.N. (2018). Role of histamine in modulating the immune response and inflammation. *Mediators Inflamm.* 2018, 9524075. <https://doi.org/10.1155/2018/9524075>.
  39. Swanton, C. (2012). Intratumor heterogeneity: Evolution through space and time. *Cancer Res.* 72, 4875–4882. <https://doi.org/10.1158/0008-5472.CAN-12-2217>.
  40. Navin, N., Kendall, J., Troge, J., Andrews, P., Rodgers, L., McIndoo, J., Cook, K., Stepansky, A., Levy, D., Esposito, D., et al. (2011). Tumour evolution inferred by single-cell sequencing. *Nature* 472, 90–94. <https://doi.org/10.1038/nature09807>.
  41. Gerlinger, M., and Swanton, C. (2010). How Darwinian models inform therapeutic failure initiated by clonal heterogeneity in cancer medicine. *Br. J. Cancer* 103, 1139–1143. <https://doi.org/10.1038/sj.bjc.6605912>.
  42. Lee, A.J.X., Endesfelder, D., Rowan, A.J., Walther, A., Birkbak, N.J., Futreal, P.A., Downward, J., Szallasi, Z., Tomlinson, I.P.M., Howell, M., et al. (2011). Chromosomal instability confers intrinsic multidrug resistance. *Cancer Res.* 71, 1858–1870. <https://doi.org/10.1158/0008-5472.CAN-10-3604>.
  43. Shah, N.P., Nicoll, J.M., Nagar, B., Gorre, M.E., Paquette, R.L., Kuriyan, J., and Sawyers, C.L. (2002). Multiple BCR-ABL kinase domain mutations confer polyclonal resistance to the tyrosine kinase inhibitor imatinib (ST1571) in chronic phase and blast crisis chronic myeloid leukemia. *Cancer Cell* 2, 117–125. [https://doi.org/10.1016/s1535-6108\(02\)00096-x](https://doi.org/10.1016/s1535-6108(02)00096-x).
  44. Roche-Lestienne, C., Soenen-Cornu, V., Grardel-Duflos, N., Laï, J.L., Philippe, N., Facon, T., Fenaux, P., and Preudhomme, C. (2002). Several types of mutations of the Abl gene can be found in chronic myeloid leukemia patients resistant to ST1571, and they can pre-exist to the onset of treatment. *Blood* 100, 1014–1018. <https://doi.org/10.1182/blood.v100.3.1014>.
  45. Mullighan, C.G., Phillips, L.A., Su, X., Ma, J., Miller, C.B., Shurtleff, S.A., and Downing, J.R. (2008). Genomic analysis of the clonal origins of relapsed acute lymphoblastic leukemia. *Science* 322, 1377–1380. <https://doi.org/10.1126/science.1164266>.
  46. Campbell, P.J., Pleasance, E.D., Stephens, P.J., Dicks, E., Rance, R., Goodhead, I., Follows, G.A., Green, A.R., Futreal, P.A., and Stratton, M.R. (2008). Subclonal phylogenetic structures in cancer revealed by ultra-deep sequencing. *Proc. Natl. Acad. Sci. USA* 105, 13081–13086. <https://doi.org/10.1073/pnas.0801523105>.
  47. Campbell, P.J., Yachida, S., Mudie, L.J., Stephens, P.J., Pleasance, E.D., Stebbings, L.A., Morsberger, L.A., Latimer, C., McLaren, S., Lin, M.-L., et al. (2010). The patterns and dynamics of genomic instability in metastatic pancreatic cancer. *Nature* 467, 1109–1113. <https://doi.org/10.1038/nature09460>.
  48. Chang, C.-H., Qiu, J., O'Sullivan, D., Buck, M.D., Noguchi, T., Curtis, J.D., Chen, Q., Gindin, M., Gubin, M.M., van der Windt, G.J.W., et al. (2015). Metabolic competition in the tumor microenvironment is a driver of cancer progression. *Cell* 162, 1229–1241. <https://doi.org/10.1016/j.cell.2015.08.016>.
  49. Berbudi, A., Rahmadika, N., Tjahjadi, A.I., and Ruslami, R. (2020). Type 2 diabetes and its impact on the immune system. *Curr. Diabetes Rev.* 16, 442–449. <https://doi.org/10.2174/1573399815666191024085838>.
  50. Andersen, C.J., Murphy, K.E., and Fernandez, M.L. (2016). Impact of obesity and metabolic syndrome on immunity. *Adv. Nutr.* 7, 66–75. <https://doi.org/10.3945/an.115.010207>.
  51. Mitchell, T.C., Hamid, O., Smith, D.C., Bauer, T.M., Wasser, J.S., Olszanski, A.J., Luke, J.J., Balmanoukian, A.S., Schmidt, E.V., Zhao, Y., et al. (2018). Epacadostat plus Pembrolizumab in patients with advanced solid tumors: Phase I results from a multicenter, open-label Phase I/II trial (ECHO-202/KEYNOTE-037). *J. Clin. Oncol.* 36, 3223–3230. <https://doi.org/10.1200/JCO.2018.78.9602>.
  52. Golkaram, M., Kuo, F., Gupta, S., Carlo, M.I., Salmans, M.L., Vijayaraghavan, R., Tang, C., Makarov, V., Rappold, P., Blum, K.A., et al. (2022). Spatiotemporal evolution of the clear cell renal cell carcinoma microenvironment links intra-tumoral heterogeneity to immune escape. *Genome Med.* 14, 143. <https://doi.org/10.1186/s13073-022-01146-3>.
  53. Love, M.I., Huber, W., and Anders, S. (2014). Moderated estimation of fold change and dispersion for RNA-seq data with DESeq2. *Genome Biol.* 15, 550. <https://doi.org/10.1186/s13059-014-0550-8>.
  54. Barbie, D.A., Tamayo, P., Boehm, J.S., Kim, S.Y., Moody, S.E., Dunn, I.F., Schinzel, A.C., Sandy, P., Meylan, E., Scholl, C., et al. (2009). Systematic RNA interference reveals that oncogenic KRAS-driven cancers require TBK1. *Nature* 462, 108–112. <https://doi.org/10.1038/nature08460>.
  55. Newman, A.M., Liu, C.L., Green, M.R., Gentles, A.J., Feng, W., Xu, Y., Hoang, C.D., Diehn, M., and Alizadeh, A.A. (2015). Robust enumeration of cell subsets from tissue expression profiles. *Nat. Methods* 12, 453–457. <https://doi.org/10.1038/nmeth.3337>.
  56. Korotkevich, G., Sukhov, V., Budin, N., Shpak, B., Artyomov, M.N., and Sergushichev, A. (2016). Fast gene set enrichment analysis. <https://doi.org/10.1101/060012>.
  57. Schliep, K.P. (2011). phangorn: Phylogenetic analysis in R. *Bioinformatics* 27, 592–593. <https://doi.org/10.1093/bioinformatics/btq706>.
  58. Lüdecke, D., Ben-Shachar, M., Patil, I., Waggoner, P., and Makowski, D. (2021). performance: An R package for assessment, comparison and testing of statistical models. *J. Open Source Softw.* 6, 3139. <https://doi.org/10.21105/joss.03139>.
  59. Bates, D., Mächler, M., Bolker, B., and Walker, S. (2015). Fitting linear mixed-effects models using lme4. *J. Stat. Soft.* 67, 1–48. <https://doi.org/10.18637/jss.v067.i01>.
  60. Halekoh, U., and Højsgaard, S. (2014). A Kenward-Roger approximation and parametric bootstrap methods for tests in linear mixed models - the

- R package pbkrtest. *J. Stat. Soft.* 59, 1–32. <https://doi.org/10.18637/jss.v059.i09>.
61. Davidson-Pilon, C. (2019). lifelines: Survival analysis in Python. *J. Open Source Softw.* 4, 1317. <https://doi.org/10.21105/joss.01317>.
  62. Schröder, M.S., Culhane, A.C., Quackenbush, J., and Haibe-Kains, B. (2011). survcomp: An R/Bioconductor package for performance assessment and comparison of survival models. *Bioinformatics* 27, 3206–3208. <https://doi.org/10.1093/bioinformatics/btr511>.
  63. Evans, A.M., DeHaven, C.D., Barrett, T., Mitchell, M., and Milgram, E. (2009). Integrated, nontargeted ultrahigh performance liquid chromatography/electrospray ionization tandem mass spectrometry platform for the identification and relative quantification of the small-molecule complement of biological systems. *Anal. Chem.* 81, 6656–6667. <https://doi.org/10.1021/ac901536h>.
  64. Dieterle, F., Ross, A., Schlotterbeck, G., and Senn, H. (2006). Probabilistic quotient normalization as robust method to account for dilution of complex biological mixtures. Application in 1H NMR metabonomics. *Anal. Chem.* 78, 4281–4290. <https://doi.org/10.1021/ac051632c>.
  65. Dobin, A., Davis, C.A., Schlesinger, F., Drenkow, J., Zaleski, C., Jha, S., Batut, P., Chaisson, M., and Gingeras, T.R. (2013). STAR: Ultrafast universal RNA-seq aligner. *Bioinformatics* 29, 15–21. <https://doi.org/10.1093/bioinformatics/bts635>.
  66. Wang, L., Wang, S., and Li, W. (2012). RSeQC: Quality control of RNA-seq experiments. *Bioinformatics* 28, 2184–2185. <https://doi.org/10.1093/bioinformatics/bts356>.
  67. Lawrence, M., Huber, W., Pagès, H., Abayoun, P., Carlson, M., Gentleman, R., Morgan, M.T., and Carey, V.J. (2013). Software for computing and annotating genomic ranges. *PLoS Comput. Biol.* 9, e1003118. <https://doi.org/10.1371/journal.pcbi.1003118>.
  68. Karolchik, D., Hinrichs, A.S., Furey, T.S., Roskin, K.M., Sugnet, C.W., Haussler, D., and Kent, W.J. (2004). The UCSC Table Browser data retrieval tool. *Nucleic Acids Res.* 32, D493–D496. <https://doi.org/10.1093/nar/gkh103>.
  69. Li, H., and Durbin, R. (2009). Fast and accurate short read alignment with Burrows-Wheeler transform. *Bioinformatics* 25, 1754–1760. <https://doi.org/10.1093/bioinformatics/btp324>.
  70. McKenna, A., Hanna, M., Banks, E., Sivachenko, A., Cibulskis, K., Kernytsky, A., Garimella, K., Altshuler, D., Gabriel, S., Daly, M., and DePristo, M.A. (2010). The Genome Analysis Toolkit: A MapReduce framework for analyzing next-generation DNA sequencing data. *Genome Res.* 20, 1297–1303. <https://doi.org/10.1101/gr.107524.110>.
  71. DePristo, M.A., Banks, E., Poplin, R., Garimella, K.V., Maguire, J.R., Hartl, C., Philippakis, A.A., del Angel, G., Rivas, M.A., Hanna, M., et al. (2011). A framework for variation discovery and genotyping using next-generation DNA sequencing data. *Nat. Genet.* 43, 491–498. <https://doi.org/10.1038/ng.806>.
  72. Koboldt, D.C., Zhang, Q., Larson, D.E., Shen, D., McLellan, M.D., Lin, L., Miller, C.A., Mardis, E.R., Ding, L., and Wilson, R.K. (2012). VarScan 2: Somatic mutation and copy number alteration discovery in cancer by exome sequencing. *Genome Res.* 22, 568–576. <https://doi.org/10.1101/gr.129684.111>.
  73. Kim, S., Scheffler, K., Halpern, A.L., Bekritsky, M.A., Noh, E., Källberg, M., Chen, X., Kim, Y., Beyter, D., Krusche, P., and Saunders, C.T. (2018). Strelka2: Fast and accurate calling of germline and somatic variants. *Nat. Methods* 15, 591–594. <https://doi.org/10.1038/s41592-018-0051-x>.
  74. Rimmer, A., Phan, H., Mathieson, I., Iqbal, Z., Twigg, S.R.F., WGS500 Consortium, Wilkie, A.O.M., McVean, G., and Lunter, G. (2014). Integrating mapping-, assembly- and haplotype-based approaches for calling variants in clinical sequencing applications. *Nat. Genet.* 46, 912–918. <https://doi.org/10.1038/ng.3036>.
  75. Larson, D.E., Harris, C.C., Chen, K., Koboldt, D.C., Abbott, T.E., Dooling, D.J., Ley, T.J., Mardis, E.R., Wilson, R.K., and Ding, L. (2012). SomaticSniper: Identification of somatic point mutations in whole genome sequencing data. *Bioinformatics* 28, 311–317. <https://doi.org/10.1093/bioinformatics/btr665>.
  76. Ellrott, K., Bailey, M.H., Saksena, G., Covington, K.R., Kandoth, C., Stewart, C., Hess, J., Ma, S., Chiotti, K.E., McLellan, M., et al. (2018). Scalable open science approach for mutation calling of tumor exomes using multiple genomic pipelines. *Cell Syst.* 6, 271–281.e7. <https://doi.org/10.1016/j.cels.2018.03.002>.
  77. McLaren, W., Gil, L., Hunt, S.E., Riat, H.S., Ritchie, G.R.S., Thormann, A., Flieck, P., and Cunningham, F. (2016). The Ensembl Variant Effect Predictor. *Genome Biol.* 17, 122. <https://doi.org/10.1186/s13059-016-0974-4>.
  78. Amemiya, H.M., Kundaje, A., and Boyle, A.P. (2019). The ENCODE blacklist: Identification of problematic regions of the genome. *Sci. Rep.* 9, 9354. <https://doi.org/10.1038/s41598-019-45839-z>.
  79. Shen, R., and Seshan, V.E. (2016). FACETS: Allele-specific copy number and clonal heterogeneity analysis tool for high-throughput DNA sequencing. *Nucleic Acids Res.* 44, e131. <https://doi.org/10.1093/nar/gkw520>.
  80. McGranahan, N., Rosenthal, R., Hiley, C.T., Rowan, A.J., Watkins, T.B.K., Wilson, G.A., Birkbak, N.J., Veeriah, S., Van Loo, P., Herrero, J., et al. (2017). Allele-specific HLA loss and immune escape in lung cancer evolution. *Cell* 171, 1259–1271.e11. <https://doi.org/10.1016/j.cell.2017.10.001>.
  81. Bindea, G., Mlecnik, B., Tosolini, M., Kirilovsky, A., Waldner, M., Obenauer, A.C., Angell, H., Fredriksen, T., Lafontaine, L., Berger, A., et al. (2013). Spatiotemporal dynamics of intratumoral immune cells reveal the immune landscape in human cancer. *Immunity* 39, 782–795. <https://doi.org/10.1016/j.jimmuni.2013.10.003>.
  82. Rooney, M.S., Shukla, S.A., Wu, C.J., Getz, G., and Hacohen, N. (2015). Molecular and genetic properties of tumors associated with local immune cytolytic activity. *Cell* 160, 48–61. <https://doi.org/10.1016/j.cell.2014.12.033>.
  83. Liberzon, A., Birger, C., Thorvaldsdóttir, H., Ghandi, M., Mesirov, J.P., and Tamayo, P. (2015). The Molecular Signatures Database (MSigDB) hallmark gene set collection. *Cell Syst.* 1, 417–425. <https://doi.org/10.1016/j.cels.2015.12.004>.
  84. Nakagawa, S., and Schielzeth, H. (2013). A general and simple method for obtaining  $R^2$  from generalized linear mixed-effects models. *Methods Ecol. Evol.* 4, 133–142. <https://doi.org/10.1111/j.2041-210x.2012.00261.x>.
  85. Schindelin, J., Arganda-Carreras, I., Frise, E., Kaynig, V., Longair, M., Pietzsch, T., Preibisch, S., Rueden, C., Saalfeld, S., Schmid, B., et al. (2012). Fiji: An open-source platform for biological-image analysis. *Nat. Methods* 9, 676–682. <https://doi.org/10.1038/nmeth.2019>.
  86. Rini, B.I., Powles, T., Atkins, M.B., Escudier, B., McDermott, D.F., Suarez, C., Bracarda, S., Stadler, W.M., Donskov, F., Lee, J.L., et al. (2019). Atezolizumab plus bevacizumab versus sunitinib in patients with previously untreated metastatic renal cell carcinoma (IMmotion151): A multi-centre, open-label, phase 3, randomised controlled trial. *Lancet.* 393, 2404–2415. [https://doi.org/10.1016/S0140-6736\(19\)30723-8](https://doi.org/10.1016/S0140-6736(19)30723-8).
  87. Motzer, R.J., Penkov, K., Haanen, J., Rini, B., Albiges, L., Campbell, M.T., Venugopal, B., Kollmannsberger, C., Negrier, S., Uemura, M., et al. (2019). Avelumab plus Axitinib versus Sunitinib for advanced renal-cell carcinoma. *N. Engl. J. Med.* 380, 1103–1115. <https://doi.org/10.1056/NEJMoa1816047>.
  88. Motzer, R.J., Tannir, N.M., McDermott, D.F., Arén Frontera, O., Melichar, B., Choueiri, T.K., Plimack, E.R., Barthélémy, P., Porta, C., George, S., et al. (2018). Nivolumab plus Ipilimumab versus Sunitinib in advanced renal-cell carcinoma. *N. Engl. J. Med.* 378, 1277–1290. <https://doi.org/10.1056/NEJMoa1712126>.
  89. Motzer, R.J., Hutson, T.E., Cella, D., Reeves, J., Hawkins, R., Guo, J., Nathan, P., Staehler, M., de Souza, P., Merchan, J.R., et al. (2013). Pazopanib versus Sunitinib in metastatic renal-cell carcinoma. *N. Engl. J. Med.* 369, 722–731. <https://doi.org/10.1056/NEJMoa1303989>.
  90. Choueiri, T.K., Powles, T., Buroto, M., Escudier, B., Bourlon, M.T., Zurawski, B., Oyervides Juárez, V.M., Hsieh, J.J., Basso, U., Shah, A.Y., et al. (2021). Nivolumab plus Cabozantinib versus Sunitinib for advanced renal-cell carcinoma. *N. Engl. J. Med.* 384, 829–841. <https://doi.org/10.1056/NEJMoa2026982>.

91. Motzer, R.J., Rini, B.I., McDermott, D.F., Redman, B.G., Kuzel, T.M., Harrison, M.R., Vaishampayan, U.N., Drabkin, H.A., George, S., Logan, T.F., et al. (2015). Nivolumab for metastatic renal cell carcinoma: Results of a randomized phase II trial. *J. Clin. Oncol.* 33, 1430–1437. <https://doi.org/10.1200/JCO.2014.59.0703>.
92. Motzer, R.J., Escudier, B., McDermott, D.F., George, S., Hammers, H.J., Srinivas, S., Tykodi, S.S., Sosman, J.A., Procopio, G., Plimack, E.R., et al. (2015). Nivolumab versus Everolimus in advanced renal-cell carcinoma. *N. Engl. J. Med.* 373, 1803–1813. <https://doi.org/10.1056/NEJMoa1510665>.
93. Viechtbauer, W. (2010). Conducting meta-analyses in R with the metafor package. *J. Stat. Soft.* 36. <https://doi.org/10.18637/jss.v036.i03>.
94. Benjamini, Y., and Hochberg, Y. (1995). Controlling the false discovery rate: A practical and powerful approach to multiple testing. *J. R. Stat. Soc. Series B Methodol.* 57, 289–300. <https://doi.org/10.1111/j.2517-6161.1995.tb02031.x>.
95. Mosteller, F., and Fisher, R.A. (1948). Questions and answers. *Am. Stat.* 2, 30. <https://doi.org/10.2307/2681650>.

## STAR★METHODS

### KEY RESOURCES TABLE

REAGENT or RESOURCE	SOURCE	IDENTIFIER
<b>Antibodies</b>		
Rabbit monoclonal GPX4	Abcam	#ab125066; RRID:AB_10973901
Mouse monoclonal CD31	Ventana-Roche	#760-4378; RRID:AB_292745
Mouse monoclonal IgG1 CD68	DAKO	#M0814; RRID:AB_2314148
<b>Deposited data</b>		
RNA-sequencing data	Golkaram et al. <sup>52</sup>	PMID: 36536472
DNA-sequencing data	Golkaram et al. <sup>52</sup>	PMID: 36536472
Metabolomics data	This paper	
<b>Software and algorithms</b>		
DESeq2	Love et al. <sup>53</sup>	PMID: 25516281
ssGSEA	Barbie et al. <sup>54</sup>	PMID: 19847166
CiberSort	Newman et al. <sup>55</sup>	PMID: 25822800
ESTIMATE	Yoshihara et al. <sup>28</sup>	PMID: 24113773
fgsea	Korotkevich et al. <sup>56</sup>	<a href="https://doi.org/10.18129/B9.bioc.fgsea">https://doi.org/10.18129/B9.bioc.fgsea</a>
phangorn	Schliep <sup>57</sup>	PMID: 21169378
performance	Lüdecke et al. <sup>58</sup>	<a href="https://doi.org/10.21105/joss.03139">https://doi.org/10.21105/joss.03139</a>
lme4	Bates et al. <sup>59</sup>	<a href="https://doi.org/10.18637/jss.v067.i01">https://doi.org/10.18637/jss.v067.i01</a>
pbkrtest	Halekoh and Højsgaard <sup>60</sup>	<a href="https://doi.org/10.18627/jss.v059.i09">https://doi.org/10.18627/jss.v059.i09</a>
lifelines	Davidson-Pilon <sup>61</sup>	<a href="https://doi.org/10.21105/joss.01317">https://doi.org/10.21105/joss.01317</a>
survcomp	Schröder et al. <sup>62</sup>	PMID: 21903630

### RESOURCE AVAILABILITY

#### Lead contact

For further information and requests for resources, please contact the lead contact, Ed Reznik ([reznike@mskcc.org](mailto:reznike@mskcc.org)).

#### Materials availability

This study did not generate new unique reagents.

#### Data and code availability

Metabolomics data generated and used in this study are published at <https://doi.org/10.5281/zenodo.7986891>. RNA and DNA sequencing data and clinical information was retrieved from Golkaram et al.<sup>52</sup> All data used to generate display items in this manuscript are available in Data S1. All original code has been deposited at [https://github.com/reznik-lab/rcc\\_coevolution](https://github.com/reznik-lab/rcc_coevolution) and is publicly available as of the date of publication. Any additional information required to reanalyze the data reported in this paper is available from the [lead contact](#) upon request.

### EXPERIMENTAL MODEL AND SUBJECT DETAILS

#### Tumor sampling

Informed consent was acquired and with Memorial Sloan Kettering Cancer Center institutional review board approval, partial or radical nephrectomies were performed at Memorial Sloan Kettering Cancer Center (New York) and stored at the MSK Translational Kidney Research Program (TKCRP). Samples were flash frozen and stored at -80 degrees Celsius until molecular characterization. Clinical metadata was recorded for all tumor samples. Samples were thawed and extracted as described in detail below, which removed proteins, dislodged small molecules bound to the protein or physically trapped in the protein matrix, and recovered a wide range of chemically diverse metabolites. Samples were then frozen, dried under vacuum, and prepared for mass spectrometry. Sex, gender, age, and other clinical data about patients in this study can be found in Golkaram et al.<sup>52</sup>

## METHOD DETAILS

### Sample preparation and metabolomic profiling

The sample extract was split in two and reconstituted in acidic and basic LC-compatible solvents where the acidic extracts were gradient eluted with water and methanol containing 0.1% formic acid, while the basic extracts, which also used water and methanol, contained 6.5 mM ammonium bicarbonate. One aliquot was analyzed using acidic positive ion optimized conditions while the second aliquot used basic negative ion optimized conditions. Two independent injections into separate dedicated columns were performed. MS and data-dependent MS/MS scans using dynamic exclusion were used alternatively to perform MS analysis. The LC/MS portion of the platform was based on a Waters ACQUITY UPLC and a Thermo-Finnigan LTQ-FT mass spectrometer, which had a linear ion-trap (LIT) front end and a Fourier transform ion cyclotron resonance (FT-ICR) mass spectrometer backend. Ions with counts greater than 2 million provided accurate mass measurements and average mass error was less than 5 ppm. Ions with fewer than 2 million counts required more effort to characterize. Fragmentation spectra (MS/MS) were typically generated in a data-dependent manner but targeted MS/MS was employed as necessary, as in the case with lower level signals.

Raw mass spectrometry files were loaded into a relational database, which was then examined and appropriate QC limits were imposed. Peaks were identified using Metabolon's proprietary peak integration software and component parts were stored in a separate data structure. An in-house library of standards from Metabolon was used to compare metabolites. Data on each of these standards were based on retention index, mass-to-charge ratio, and MS/MS spectra. For each compound in the metabolomic data, parameters were compared to analogous parameters in the standard library. As described in Evans et al.,<sup>63</sup> compounds were identified based on three criteria: retention index within 75 RI units of the proposed identification, mass within 0.4 m/s, and MS/MS forward and reverse match scores.

### Data normalization

Block normalization was performed when metabolomics data was measured across several days. Each compound was corrected in run-day blocks by registering the medians to equal one and normalizing each data point accordingly. The minimal measured level of a metabolite across all samples was imputed when metabolite levels were below the detection limit. Probabilistic quotient normalization was then performed, accounting for an overall estimation on the most probable dilution factor.<sup>64</sup> Data was then log<sub>2</sub>-transformed.

### Necrosis pathology review

Hematoxylin and eosin (H&E) stained slides were reviewed for morphologic features including coagulative-type necrosis (Figure S2G). Extent of tumor necrosis was subjectively quantified by a pathologist (SG) for all cases that were reviewed.

### Whole transcriptome sequencing

Extracted RNA samples were quantified with Qubit RNA HS assay Kit, and 100 ng of RNA was used for each library preparation input with Illumina TruSeq Stranded Total RNA with Ribo-zero. Each resulting library was quantified individually with Qubit dsDNA HS Kit and normalized to 4 nM prior to sequencing. RNA sequencing libraries were prepared in batches of 24, with each individual RNA sample uniquely indexed using Illumina TruSeq RNA UD Indexes. Final libraries were pooled for sequencing in up to 36-plex on NovaSeq 6000 S2 flow cell, or up to 72-plex on NovaSeq 6000 S4 flow cell. All RNA samples in the cohort were selected for library preparation and sequencing. Each sample was assigned a unique identifier during sample accessioning to prevent sample selection bias. A paired-end 76 base pair sequencing recipe was used to produce ~200 million total paired reads per sample. Batch effects were not observed (Figure S6A).

### RNA-seq data processing pipeline

STAR 2-pass alignment<sup>65</sup> was used to align RNA-sequencing reads against human genome assembly hg19. Numerous QC metrics, such as general sequencing statistics, gene feature, and body coverage, were calculated through RSeQC<sup>66</sup> based on the alignment result. The R package GenomicAlignments<sup>67</sup> aligned reads with UCSC KnownGene<sup>68</sup> in hg19 as the base gene model was used to compute raw RNA-seq gene level count values. Union counting mode was used and mapped paired reads after alignment quality filtering was used. Finally, the R package DESeq2<sup>53</sup> was utilized to estimate the sample size factor (using the estimateSizeFactors function), and to generate the sample size normalized read count matrix (using the counts function). DESeq2's fpkm function was then used to generate the FPKM normalized values which were derived based on the sample size normalized counts along with the gene model used in raw count quantification.

### Whole-exome sequencing

40ng input of DNA per sample was used to generate libraries for whole-exome sequencing with TruSight Oncology DNA Library Prep Kit, and TruSight Oncology index PCR products were used for enrichment. Target exome enrichment was performed using the IDT xGen Universal Blockers and IDT xGen Exome Research High Sensitivity assay (Biotium) was used for library quantification of the post-enriched libraries. Libraries were normalized post-enrichment using bead-based normalization and pooled. Illumina NovaSeq™ 6000 S4 flow cell using the XP workflow for individual lane loading (12-plex per lane) was used to sequence samples using 101 bp paired-end reaches. Each sample yielded an average of 500 million reads and a median target coverage depth of 360X. No differences in TMB were observed between batches (Figure S6B).

### WES data processing pipeline

Alignment of raw sequencing data to the hg19 genome build was performed using Burrows-Wheeler Aligner (BWA) version 0.7.17.<sup>69</sup> Genome Analysis Toolkit (GATK) version 3.8<sup>70</sup> was used following raw reads alignment guidelines from DePristo et al.<sup>71</sup> to realign indels, recalibrate base-quality scores, and remove duplicate reads. Small variant calling was performed using VarScan 2,<sup>72</sup> Strelka v2.9.10,<sup>73</sup> Platypus 0.8.1,<sup>74</sup> Mutect2 - part of GATK 4.1.4.1,<sup>71</sup> and SomaticSniper version 1.0.5.0 (SNVs only).<sup>75</sup> Variants called by a combination of 2 out of 5 callers are reported, following recommendations from the Cancer Genome Atlas Research Network.<sup>76</sup> The following criteria were used to filter variants:

- (1) Tcov > 10 and Taf >= 0.4, Ncov > 7 and Naf <= 0.01, Tac > 4.
- (2) Common SNPs were identified by.snp142.vcf and eliminated.
- (3) Rare variants identified in dbSNP are kept if Naf = 0.
- (4) Low confidence variants had Tcov < 20 or Tac < 4.
- (5) Variants must be called by more than a combination of 2 or more callers.
- (6) Common variants were identified by gnomAD v2.1.1 and excluded.

Variants were annotated using Variant Effect Predictor (VEP).<sup>77</sup> As per Amemiya et al.,<sup>78</sup> INDELS in blacklisted and/or low mappability regions (such as repeat regions) were excluded. FACETS v.6.1<sup>79</sup> was used to perform allele-specific copy number analysis while allele-specific HLA loss of heterozygosity was determined using LOHHHLA as described by McGranahan et al.<sup>80</sup>

### Bulk RNA-seq deconvolution analysis

Immune features and signature gene lists of immune cell types were obtained according to Bindea et al.<sup>81</sup> and Senbabaoğlu et al.<sup>3</sup> ssGSEA<sup>54</sup> and Cibersort<sup>55</sup> methods were used for bulk RNA-seq deconvolution analysis. ssGSEA takes FPKM values as its input and calculates enrichment scores for given gene lists compared to all other genes in the sample's transcriptome. Cibersort also uses FPKM expression values as its input but has its own published LM22 gene expression matrix of immune cell types of interest, which it uses as a reference to compute the infiltration level of each immune cell type. Based on the work of Rooney et al.,<sup>82</sup> immune cytolytic score ('CYT') was calculated using the geometric mean of TPM (transcripts per million) of granzyme A (GZMA) and perforin (PRF1), two cytolytic effector genes. Immune Score, Stromal Score, and ESTIMATE Score were calculated through the estimate R package.<sup>28</sup> Along with the Angiogenesis score published by Masiero et al.,<sup>31</sup> the role of stromal and immune compartments in the tumor microenvironment were dissected.

### Bulk gene set enrichment analysis

DESeq2 was used to test for differential expression using negative binomial generalized linear models. T-statistics derived from differential expression analysis using DESeq2 were fed into the fgsea package (which expects ranked statistics) in order to run gene set enrichment analysis.

Ranked gene set enrichment analysis (GSEA) was run on all genes using the t-statistic calculated from the DESeq2 package. 50 gene sets based on Hallmark<sup>83</sup> were used. GSEA analysis was performed using the fgsea function from the fgsea R package (v1.18).<sup>56</sup>

### Metabolomics and RNA ITH scores

Gene- and patient-wise intra-patient heterogeneity scores were calculated using multiregion data. Data was first median-centered to remove any metabolite/gene-level bias. For each metabolite/gene, the difference between each pair of samples from the same tumor were calculated. The median difference between the paired-differences was taken, yielding a metabolite/gene-specific, patient-specific measure of heterogeneity. This was repeated for all metabolites/genes, across all tumors, generating a matrix of metabolite/gene by patient values. Metabolite/gene intratumor heterogeneity values are summarized as the median value per metabolite/gene across all tumors in the cohort. Patient intratumor heterogeneity values are summarized as the median value per tumor across all metabolites/genes. Patient intratumor heterogeneity values represent the expected value of the absolute log<sub>2</sub>-fold change for a randomly chosen metabolite/gene within a given tumor. This measure of heterogeneity is not biased by the number of multiregion samples per tumor (Spearman correlation p-value = 0.23 in metabolomics, Spearman correlation p-value = 0.15 in transcriptomics) (Figure S6C). Inter-patient heterogeneity scores were calculated by taking the difference between each pair of samples from all other patients.

### DNA ITH scores

For each pair of regions, the percentage of unique mutations between regions from a patient and across patients was calculated. Genetic ITH scores for each patient were defined as the median proportion of private somatic mutations (SNVs and INDELs) not shared between regions from a single patient, equivalent to 1-Jaccard Similarity Index. Here, a score of 0/1 corresponded to complete overlap/complete lack of overlap in mutational profiles. Similar to RNA/metabolomics ITH scores, this measure of heterogeneity is not biased by the number of multiregion samples per tumor (Spearman correlation p-value = 0.72) (Figure S6).

### Differential abundance score

The differential abundance (DA) score evaluates whether a metabolic pathway is differentially regulated between two groups. First, a Wilcoxon rank sum test was applied to all metabolites. P-values were then corrected using the Benjamini-Hochberg method (FDR-adjusted p-value < 0.05). The DA score for each pathway is calculated as: (#significantly enriched metabolites - #significantly depleted metabolites)/ #total metabolites. Only pathways with 3 or more significantly altered metabolites were scored.

### Robinson-Foulds distance

Robinson-Foulds distances in Figures 2I and 2J were calculated using the phangorn R package (v2.8.1).<sup>57</sup> To calculate the Robinson-Foulds distance between two trees ( $T_1$  and  $T_2$ ) with  $n$  tips:

$$d(T_1, T_2) = i(T_1) + i(T_2) - 2v_s(T_1, T_2)$$

where  $i(T_1, T_2)$  represents the number of internal edges and  $v_s(T_1, T_2)$  represents the number of shared internal splits. The reported Robinson-Foulds distance is calculated by dividing  $d(T_1, T_2)$  by the maximal possible distance  $i(T_1) + i(T_2)$  to get a normalized distance.

### GPX4 immunohistochemistry

Immunohistochemistry for glutathione peroxidase 4 (GPX4) was performed in 5 µm FFPE tissue sections using an automated staining system (Leica Bond RX) with 3,3' diaminobenzidine detection (Figures 3H and 3I). Antigen retrieval was conducted for 30 mins using Leica Bond epitope retrieval solution 1 (ER1; citrate, pH 6; cat. #AR9961), followed by an incubation with a rabbit monoclonal GPX4 antibody (EPNCIR144, Abcam, #ab125066, dilution 1:1200) for 30 min, and a subsequent incubation of the secondary antibody (Leica Bond Polymer Refine Detection cat. #DS9800). GPX4 staining was quantified as H-Scores [H= intensity (0-3) x percentage of positive cells (1-100)] by a pathologist (YBC) who was blinded to the metabolite levels of the samples.

### Linear mixed modelling of immune phenotypes

A linear regression was performed where metabolite levels were used to predict immune signature expression. To account for repeated measures, a linear mixed model was used, with a random effect for each patient. Marginal  $r^2$  was calculated to consider only the variance of the fixed effects.<sup>84</sup> Functions from performance<sup>58</sup> and lme4<sup>59</sup> packages were used to conduct the modelling. To assess significance, parametric bootstrapping was performed with 100,000 iterations using the pbkrtest package.<sup>60</sup>

The following equations were used to fit the linear mixed models.

Actual model : Metabolite ~ ImmuneSignature + (1 | Patient)

Null model : Metabolite ~ (1 | Patient)

### Immunofluorescence for CD31 and CD68

Immunofluorescence detections of CD31 and CD68 (Figures 5A–5C) was performed by the Molecular Cytology Core Facility at Memorial Sloan Kettering Cancer Center using Discovery Ultra processor (Ventana Medical Systems.Roche-AZ). Heat and CC1 (Cell Conditioning 1, Ventana cat #950-500) retrieval were performed for 32 min. The tissue sections were then blocked for 30 min in Background Blocking reagent (Innovex, catalog#: NB306). Next, a mouse monoclonal anti-CD31 primary antibody (Ventana-Roche, cat#760-4378) was incubated for 5 h, followed by a 16-min secondary antibody incubation of biotinylated anti-mouse secondary (Vector Labs, MOM Kit BMK-2202) in 5.75 ug/mL Blocker D, Streptavidin-HRP, and TSA Alexa488 (Life Tech, cat#B40932) prepared according to manufacturer instructions in 1:150. 0.02 ug/mL of a mouse monoclonal IgG1 anti-CD68 antibody (DAKO, cat#M0814) was used and incubated for 5 h, followed by a 16-min secondary incubation using a biotinylated goat anti-mouse secondary antibody (Vector Labs, MOM Kit BMK-2202) in 5.75 ug/mL. Blocker D, Streptavidin-HRP, and CF 543 (Biotium, cat#92172) were prepared according to manufacturer instructions in 1:500. To counterstain, 5ug/mL of DAPI [dihydrochloride(2-(4-Amidinophenyl)-6-indolecarbamidine dihydrochloride] (Sigma D9542) was used for 5 min at room temperature. The tissue was then mounted with anti-fade mounting medium Mowiol [Mowiol 4-88 (CALBIOCHEM code: 475904)] and coverslipped.

To scan slides, a Pannoramic P250 Flash scanner (3DHistech, Hungary) with 20x/0.8NA objective lens was used. CaseViewer software (3DHistech, Hungary) was used to visualize digitized images. One representative region of interest (ROIs) was selected for CD31 and CD68 and then exported as.tif files. Regions were analyzed using ImageJ/Fiji software (v2.1.0; NIH USA).<sup>85</sup>

### Imputation of metabolites by RNA with MIRTH

MIRTH (Metabolite Imputation via Rank-Transformation and Harmonization) is a method to impute missing metabolites by jointly modeling metabolite covariation across heterogeneously covered metabolomics datasets.<sup>37</sup> Intuitively, MIRTH operates by learning the covariation between metabolite and transcript levels in a reference dataset where both are measured and then transferring that knowledge to other datasets where metabolites are unmeasured.

Before applying MIRTH, the metabolomics data in each dataset are preprocessed by total ion count (TIC) normalization and transcripts levels are transformed into units of TPM (Transcripts Per Million). Metabolomics and transcriptomics are then

rank-transformed, resulting in values between 0 and 1 for each feature across all samples in a batch. Preprocessed metabolomics and transcriptomics data are then aggregated into a single aggregate multiple-dataset matrix  $\mathbf{X}$ , which then undergoes nonnegative matrix factorization (NMF). As described in detail in Freeman et al.,<sup>37</sup> MIRTH implements a modified NMF which omits missing data from the element-wise objective function. Optimization produces two embedding matrices W and H which are full rank and whose product yields a new matrix  $\hat{\mathbf{X}}$  with no missing data. Ten-fold cross validation is used to determine the optimal number of embedding dimensions.

Three ccRCC datasets with paired metabolomics and transcriptomics data: M1 (N=32), M4 (N=144), and M5 (N=76) were used to assess MIRTH's performance ([Figure S5A](#)). For each dataset, we repeated the following procedure. We masked metabolites in the "target" dataset treating them as effectively missing. We then trained a MIRTH model (where the input data contained both metabolites and RNA from non-target datasets and RNA data only from the target dataset), and then calculated imputed metabolite levels from the target dataset. We repeated such experiments 10 times with different seeds to remove random bias. Finally, we compared for each (sample,metabolite) pair the average of imputed metabolite values by MIRTH with the true metabolite values in the testing set by calculating Spearman's rank correlation coefficient. Metabolites that satisfied criteria for statistical significance (FDR-adjusted p-value < 0.05, average rho > 0.3) were defined as well-predicted in that dataset ([Figure S5B](#)). For instance, 1-methylimidazole acetate and 2-amino adipate were reproducibly well-predicted with an average rho of 0.67 and 0.51 across 3 datasets respectively ([Figure S5C](#)). Metabolites that were well-predicted in at least 2 datasets are defined as reproducibly well-predicted. This yielded 262 reproducibly well-predicted metabolites.

### Survival analysis

We collected RNA sequencing data and patient-level clinical data from 7 published trials of immunotherapeutic vs systemic agents in advanced ccRCC (IMmotion151 (N=823), NCT02420821<sup>86</sup>; JAVELIN Renal 101 (N=726), NCT02684006<sup>87</sup>; CheckMate 214 (N=167), NCT02231749<sup>88</sup>; COMPARZ (N=412), NCT00720941<sup>89</sup>; CheckMate 9ER (N=16), NCT03141177<sup>90</sup>; CheckMate 010 (N=45), NCT01354431<sup>91</sup>; CheckMate 025 (N=248), NCT01668784<sup>92</sup>).

Considering the different drug effect of treatments in clinical trials, we performed statistical analysis on immuno-therapy arms and sunitinib arms separately (Immuno-therapy drugs: Avelumab + Axitinib, Atezolizumab + Bevacizumab, Nivolumab, Ipilimumab + Nivolumab). For the 262 reproducibly well-predicted metabolites, we tested the association between levels of individual metabolites and progression free survival (PFS) in a multivariate Cox proportional-hazards model (adjusted by age and sex; PFS ~ metabolite level + age + gender). The Python package lifelines<sup>61</sup> was used for survival regression. Regression results across multiple clinical trials were then aggregated by a meta-analysis method, restricted maximum likelihood (REML) random effects model in R package metafor.<sup>93</sup> All p-values were Benjamini-Hochberg corrected.<sup>94</sup>

## QUANTIFICATION AND STATISTICAL ANALYSIS

### Statistical analysis

All statistical tests were performed in R. Tests comparing distributions were performed using wilcox.test or t.test. All statistical analyses were two-sided, unless otherwise specified, and p-values were Benjamini-Hochberg corrected.<sup>94</sup> The survcomp package<sup>62</sup> was used to perform the meta-analysis to combine results from the two metabolomic batches using Fisher's method.<sup>95</sup>

### ADDITIONAL RESOURCES

Normalized metabolomics data matrices and sample information can be found at <https://doi.org/10.5281/zenodo.7986891>.